SIGNAL PREDICTION FOR MAGNETIC PARTICLE IMAGING USING A MODEL-BASED DICTIONARY APPROACH

A THESIS SUBMITTED TO

THE GRADUATE SCHOOL OF ENGINEERING AND SCIENCE

OF BILKENT UNIVERSITY

IN PARTIAL FULFILLMENT OF THE REQUIREMENTS FOR

THE DEGREE OF

MASTER OF SCIENCE

IN

ELECTRICAL AND ELECTRONICS ENGINEERING

By

Aslı Alpman

July 2023

Signal Prediction for Magnetic Particle Imaging Using a Model-Based Dictionary Approach
By Aslı Alpman
July 2023

We certify that we have read this thesis and that in our opinion it is fully adequate, in scope and in quality, as a thesis for the degree of Master of Science.

Emine Ülkü Sarıtaş Çukur(Advisor)

Tolga Çukur

Nevzat Güneri Gençer

Approved for the Graduate School of Engineering and Science:

Orhan Arıkan
Director of the Graduate School

ABSTRACT

SIGNAL PREDICTION FOR MAGNETIC PARTICLE IMAGING USING A MODEL-BASED DICTIONARY APPROACH

Aslı Alpman
M.S. in Electrical and Electronics Engineering
Advisor: Emine Ülkü Sarıtaş Çukur
July 2023

Magnetic particle imaging (MPI) is a tracer-based medical imaging technique that enables quantification and spatial mapping of magnetic nanoparticle (MNP) distribution. The magnetization response of MNPs depends on both experimental conditions such as drive field (DF) settings and viscosity of the medium, and the magnetic parameters such as magnetic core diameter, hydrodynamic diameter, and magnetic anisotropy constant. A comprehensive understanding of the magnetization response of MNPs can facilitate the optimization of DF and MNP type for a given MPI application. This thesis proposes a calibration-free algorithm using model-based dictionaries for MNP signal prediction at untested experimental conditions. The proposed algorithm also incorporates non-model-based dynamics by modeling them as a linear time-invariant system. These dynamics include the system response of the measurement setup as well as the magnetization dynamics not accounted for by the employed coupled Brown-Néel rotation model, such as dipolar interactions and non-uniaxial magnetic anisotropy. The proposed iterative calibration-free algorithm simultaneously estimates the dictionary weights and the transfer functions due to non-model based dynamics. Experiments on in-house magnetic particle spectrometer (MPS) setup demonstrate that the proposed algorithm successfully predicts the MNP signals at untested viscosities within the biologically relevant range, as well as at untested DF settings.

Keywords: Magnetic particle imaging, signal prediction, magnetic nanoparticles, coupled Brown-Neél rotation model, magnetization response, model-based dictionary, inverse problem, alternating minimization.

ÖZET

MODELE DAYALI SÖZLÜK YAKLAŞIMI İLE MANYETİK PARÇACIK GÖRÜNTÜLEME İÇİN SİNYAL TAHMİNİ

Aslı Alpman
Elektrik ve Elektronik Mühendisliği, Yüksek Lisans
Tez Danışmanı: Emine Ülkü Sarıtaş Çukur
Temmuz 2023

Manyetik parçacık görüntüleme (MPG), manyetik nanoparçacık (MNP) dağılımının miktarının belirlenmesini ve uzamsal haritalanmasını sağlayan izleyici tabanlı bir tıbbi görüntüleme tekniğidir. MNP'lerin manyetizasyon tepkisi, eksitasyon alanı (EA) ayarları ve viskozitesi gibi deneysel koşullara ve manyetik çekirdek çapı, hidrodinamik çap ve manyetik anizotropi sabiti gibi manyetik parametrelere bağlıdır. MNP'lerin manyetizasyon tepkisinin kapsamlı bir şekilde anlaşılması, belirli bir MPG uygulaması için EA ve MNP tipinin optimizasyonunu kolaylaştırabilir. Bu tez, test edilmemiş deneysel koşullarda MNP sinyal tahmini için modele dayalı sözlükler kullanarak, kalibrasyon gerektirmeyen bir algoritma önermektedir. Önerilen algoritma aynı zamanda model tabanlı olmayan dinamikleri bir doğrusal zamanda değişmez sistem olarak modelleyerek göz önünde bulundurur. Bu dinamikler, ölçüm düzeneğinin sistem yanıtını ve kullanılan akuple Brown-Néel dönüş modeli tarafından açıklanmayan dipolar etkileşimler ve tek eksenli olmayan manyetik anizotropi gibi manyetizasyon dinamiklerini içerir. Önerilen yinelemeli kalibrasyonsuz algoritma, sözlük ağırlıklarını ve model tabanlı olmayan dinamikleri modelleyen transfer fonksiyonlarını aynı anda tahmin eder. Manyetik parçacık spektrometresi (MPS) düzeneğinde gerçekleştirilen deneyler, önerilen algoritmanın MNP sinyallerini biyolojik olarak ilgili aralık içindeki test edilmemiş viskozitelerde ve ayrıca test edilmemiş EA ayarlarında başarılı bir şekilde tahmin ettiğini göstermektedir.

Anahtar sözcükler: Manyetik parçacık görüntüleme, sinyal tahmini, manyetik nanoparçacıklar, akuple Brown-Neél dönüş modeli, manyetizasyon tepkisi, modele dayalı sözlük, ters problem, dönüşümlü minimizasyon.

Acknowledgement

First of all, I would like to thank my advisor, Assoc. Prof. Emine Ülkü Sarıtaş, for her invaluable guidance and support. I have gained immense knowledge and insights from her expertise in the field. Her role in my academic journey goes far beyond that of an advisor, as she became a constant source of inspiration and a role model for me.

I would also like to thank Assoc. Prof. Tolga Çukur and Prof. Nevzat Güneri Gençer for being on my master's thesis committee. I greatly valued and deeply appreciated their feedback on my work.

I would like to thank the Scientific and Technological Research Council of Turkey (TUBITAK Grant No: 120E208, 217S069, 120E346) for its support to this thesis.

I would like to thank Prof. Jürgen Weizenecker for his invaluable feedback on the solution of coupled Brown-Néel model.

I would like to thank my colleagues in our research group: Beril Alyüz, Bahadır Alp Barlas, Elif Aygün, Ecrin Yağız, Mustafa Utkur, Abdallah Zaid Alkinali, Atakan Topçu, Ege Kor and Musa Tunç Arslan. I especially would like to thank Beril, who has been my closest friend and a source of encouragement during moments of despair. I would also like to acknowledge the invaluable support and guidance provided by Bahadır, Elif, and Ecrin. Bahadır has been a source of exceptional support, lifting my spirits whenever I felt discouraged. Elif has always been friendly and answered my question tirelessly. Ecrin has been a guiding presence in my life since high school. Atakan, my neighbor in both UMRAM and grad apartments, always exuded positivity and support. Mustafa helped me a lot in learning experimental procedures and facilitated my adaptation to the laboratory environment.

I would like to thank my brother, Utku Alpman, and his wife, Tuğçe Nur Alpman, for their endless support and love. They bring immense joy to my life.

I cherish the moments we share together, filled with laughter and love.

Finally, I would like to thank my mother, Tamay Alpman. Her belief in me is the greatest source of motivation and confidence to pursue my dreams and overcome challenges. Her support has shaped the person I am today, and I am forever grateful for her presence in my life.

Contents

List of Figures

Chapter 1

Introduction

Magnetic particle imaging (MPI) is a biomedical imaging modality that allows quantification and spatial mapping of magnetic nanoparticle (MNP) distribution with high resolution and sensitivity [1, 2, 3, 4, 5]. MPI has a variety of applications including stem cell tracking [6, 7, 8, 9], angiography [10, 11, 12], cancer imaging [13, 14, 15], localized hyperthermia [16, 17, 18], interventional imaging [19, 20, 21], inflammation imaging [22, 23], and viscosity and/or temperature estimation [24, 25].

MPI uses an oscillating drive field (DF) to generate a time-varying magnetization response for non-saturated MNPs inside a field free region (FFR), which in turn induces a signal on the receiver coil. Two main mechanisms govern the magnetization dynamics of MNPs, the Néel and Brownian processes [26, 27, 28]. In the Néel process, the magnetic moment of the MNP internally aligns itself with the applied field without any physical rotation. This process is affected by the MNP characteristics, such as magnetic core diameter, magnetic anisotropy originating from the shape and crystal structure of the MNP, as well as the temperature of the local environment. In the Brownian process, the MNP physically rotates to align its magnetic moment with the applied field. This process is affected by the MNP properties, such as core and hydrodynamic diameter, as well as the viscosity and temperature of the local environment. Brownian and Néel mechanisms occur in a coupled fashion, where magnetic moment rotation and physical rotation of the particle affect each other. Besides these two mechanisms, interparticle magnetodipolar interactions can significantly affect the overall magnetization behavior [29, 30, 31, 32, 33, 34].

For applications of MPI such as temperature and viscosity mapping, the optimal DF settings depend on MNP type and need to be determined via extensive experiments [25]. A better understanding of MNP magnetization dynamics can enable the optimization of DF and/or MNP type for a given application. Various theoretical models describing the magnetization dynamics of MNPs have been proposed and used in simulation studies to understand and explain the experimental results in MPI [35, 36, 37, 38, 39, 40, 41, 42, 43, 44, 45, 46, 47, 48]. Some studies decouple the Brownian and Néel processes by inhibiting or neglecting one of these processes. Examples of decoupling include immobilizing MNPs to inhibit the Brownian process [45, 46], assuming the Brownian rotation is neglectable once the easy axis is aligned with the field direction [38], or ignoring Néel rotation under small viscosity and strong anisotropy [39]. Recently, some studies utilized the Néel rotation model to create model-based dictionaries containing simulated signals for MNPs with different magnetic properties. These dictionaries were then employed for magnetic parameter estimation via data fitting to the MPS measurements [45] or system matrix measurements [46], with the future goal of achieving model-based system calibration. However, the models that consider the interdependence between Néel and Brownian rotations are favorable for a more realistic understanding of MNP magnetization dynamics. A recent study presented an important step in this direction by deriving coupled differential equations for particle and magnetic moment rotation and transforming them into a system of ordinary differential equations (ODE) where a numerical solution is possible [47].

This thesis proposes a calibration-free iterative dictionary-based algorithm that uses the coupled Brown–Néel rotation model, with the goal of predicting the MNP signal. The proposed approach simultaneously estimates the dictionary weights and the non-model based dynamics based on available measurements, and utilizes this information to predict the MNP signal at untested experimental conditions, such as untested viscosities or untested DF settings. Consequently, the proposed algorithm accounts for model based dynamics, as well as the system and magnetization dynamics that the model can not explain. Using magnetic particle spectroscopy (MPS) experiments performed in the biologically relevant viscosity range of 0.89-15.33 mPa·s and DF frequencies between 0.25-2 kHz, this thesis shows that the proposed approach can successfully predict the MNP signals at untested settings.

Chapter 2

Background and Theory

2.1 Magnetic Particle Imaging (MPI)

MPI uses permanent magnets or electromagnets to create a zero-field region, as depicted in Fig. 2.1(a). This field free region (FFR) can be a field-free point (FFP), or a field-free line (FFL), depending on the magnet configuration. This static and position-dependent magnetic field is known as the selection field and saturates the magnetization of the MNPs outside the FFR due to the non-zero magnetic field. As described in Section 2.3.1 below, the magnetization response of MNPs can be modeled using the Langevin function $\mathcal{L}$ as follows:

$$M = \mu\rho\mathcal{L}(\xi) \tag{2.1}$$

where

$$\mathcal{L}(\xi) = \coth(\xi) - \frac{1}{\xi} \tag{2.2}$$

Here, M [A/m] is the magnetization amplitude in the applied field direction, μ [Am^2] dipole magnetic moment amplitude, and ρ [particles/m^3] is the particle density. The Langevin function takes unitless $\xi = \frac{\mu B}{k_B T}$ as its argument, where B [T] is the applied magnetic field amplitude, k_B is the Boltzmann constant, and T [K] is the temperature. As shown in Fig. 2.1(b), when ξ gets larger (i.e., for

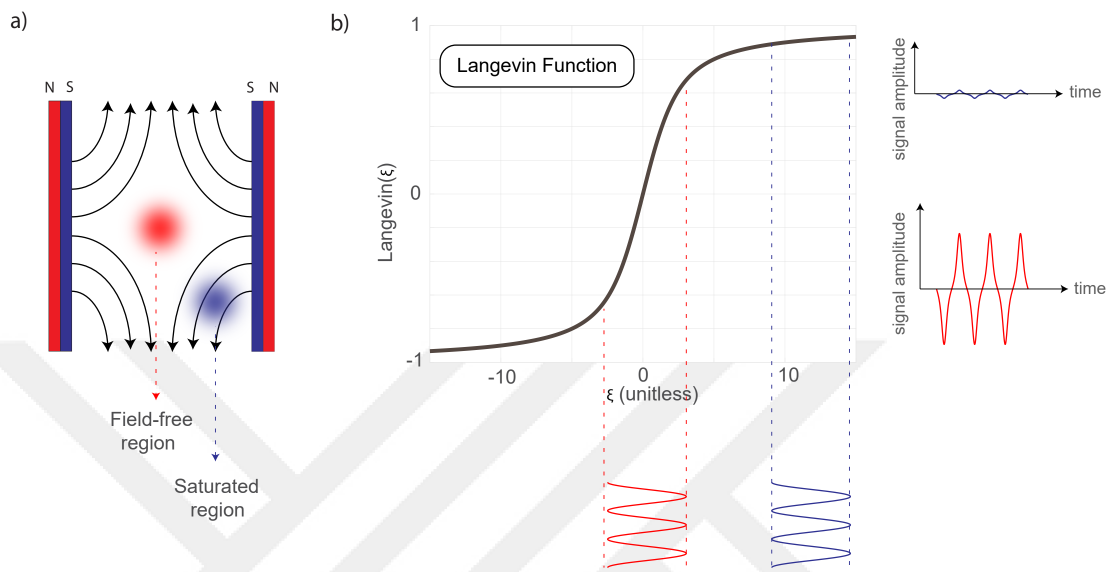

Figure 2.1: *(a) A schematic of the MPI scanner showing the field-free region (FFR) and saturated region. Permanent magnets or electromagnets create a FFR at the center while creating strong fields in other areas, namely saturated regions, to saturate the magnetization of the MNPs. (b) Applied drive fields and the resulting induced signals due to the magnetization change. The magnetization change is insignificant for saturated regions, and thus the signal amplitude is relatively small. The main signal, on the other hand, originates from the FFR, allowing signal localization for MPI.*

larger applied fields), the magnetization of the MNPs saturate, as in the case of MNPs outside the FFR.

When a sinusoidal drive field (DF) is superimposed on the selection field, it causes a time-varying magnetization response of non-saturated MNPs inside the FFR. This change in the magnetization induces a voltage on the receiver coil. Since the MNPs outside the FFR are saturated, their magnetization does not significantly change with the applied DF, as illustrated in Fig. 2.1(b). Therefore, the MNPs outside the FFR do not contribute to the induced voltage, which enables signal localization in MPI.

In MPI, the static and position-dependent selection field can be written for the one-dimensional case as follows:

$$B_s(x) = -Gx \tag{2.3}$$

where G [T/m] is the gradient strength and x [m] is the position relative to the FFP. Note that $x = 0$ at the FFP position. Then, a position-independent sinusoidal DF is applied to excite MNPs at the field-free region, which has the following formula:

$$B_d(t) = B_p cos(2\pi f_d t) \tag{2.4}$$

where B_p [T] denotes the peak DF amplitude and f_d [Hz] denotes DF frequency. Superimposing selection field and DF, we have the following total field at a position x and time t:

$$B(x,t) = B_p cos(2\pi f_d t) - Gx \tag{2.5}$$

One can find the time-dependent FFP position, $x_s(t)$, by solving $B(x,t) = 0$, which yields:

$$\begin{aligned} B_d(t) - Gx_s(t) &= 0 \\ x_s(t) &= \frac{B_d(t)}{G} \end{aligned} \tag{2.6}$$

Accordingly, the FFP position is determined by the applied DF and selection field. The received signal can be converted to an MPI image with two different methods, which are (1) system function reconstruction (SFR) and (2) the x-space reconstruction. SFR requires a pre-calibration of the scanner, where the measured signals of point-like samples at all grid positions within the field-of-view (FOV) are stacked in a system matrix [49]. Then, an inverse problem is formulated to express the MPI signal, coming from the volume of interest, as a weighted linear combination of system matrix columns. The weight solution gives the underlying MNP distribution image of the volume of interest. While the SFR method can generate high-resolution images, it requires time-consuming acquisition of the system matrix for calibration. In contrast, the x-space approach facilitates the mapping of the acquired MPI signal to the image coordinates after a speed compensation step [4]. If the point spread function (PSF) is known or measured, the resolution of the x-space reconstructed image can be further improved via post-processing.

2.2 Magnetic Particle Spectroscopy (MPS)

Magnetic Particle Spectroscopy (MPS), also known as Magnetic Particle Relaxometry or Magnetization Response Spectroscopy, is a zero-dimensional MPI system that only utilizes time-changing magnetic fields to excite the MNPs. Unlike MPI, MPS does not employ static gradient fields to saturate the MNPs, meaning that FFP extends to the whole sample chamber, as shown in 2.2(b). Due to having high sensitivity and low cost, MPS has been used in diverse applications such as bioassays [50, 51, 52], viscosity and temperature mapping [53, 24], blood analysis [54, 55], and, cell labeling and tracking [56, 57, 58, 59]. Additionally, Arbitrary Waveform (AW) MPS setups that can work with arbitrary DF waveform without requiring impedance matching have become a powerful tool for magnetic characterization [60]. The drive coil in these setups are designed to have low inductance and hence have low impedance in a wide range of frequencies.

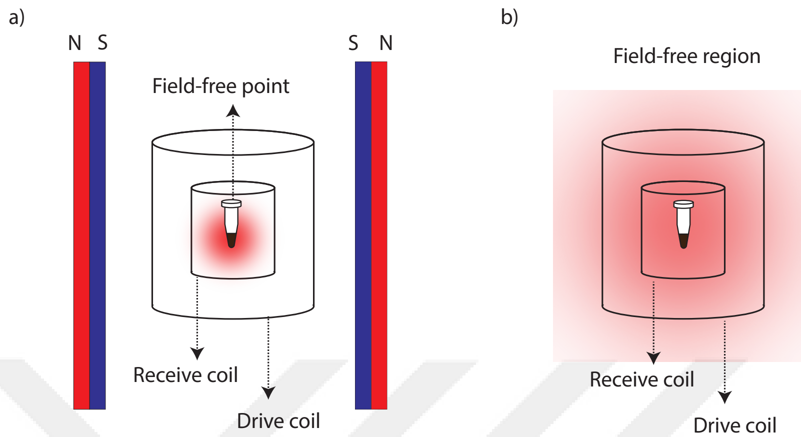

Figure 2.2: *A comparison for MPI and MPS instrumentations. (a) A conventional MPI scanner consists of magnets that generate a gradient field utilized as the selection field. It also includes a drive coil to produce a drive field and receive coil to pick up the induced signal. Due to the presence of the magnets, the size of the field-free region is small. (b) Unlike MPI scanners, MPS does not contain magnets creating the selection field. Hence, field free region extends to the whole sample chamber.*

2.3 Magnetic Nanoparticle (MNP) Dynamics

2.3.1 The Adiabatic Model: Langevin Function

MPI utilizes the nonlinear magnetic response of magnetic nanoparticles (MNPs), typically consisting of superparamagnetic iron oxides (SPIONs). The adiabatic model assumes that the magnetization changes much more slowly than the relaxation of the MNPs, meaning that the magnetization is at equilibrium at each time step [61]. Assuming that the MNPs are non-interacting, magnetically isotropic, and can be modeled as a dipole, we have the following energy formula for each single MNP under an applied magnetic field $\boldsymbol{B}$:

$$E = -\boldsymbol{\mu} \cdot \boldsymbol{B} \tag{2.7}$$

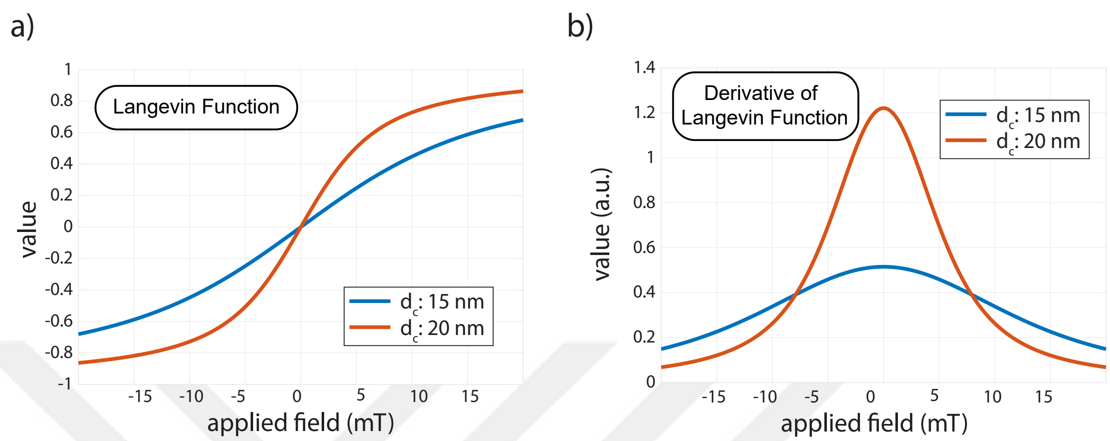

Figure 2.3: *The adiabatic magnetization dynamics, characterized by the Langevin function, depends on the core volume. (a) The Langevin curve gets sharper as the core diameter (d_c) and, thus, the core volume (V_c) increases. (b) The derivative of the Langevin curve, which is closely related to the induced MPI signal, also gets sharper for larger core volume.*

Here, $\boldsymbol{\mu} = \mu \boldsymbol{m}$ with $\boldsymbol{m}$ is the unit vector representing the dipole magnetic moment direction. Note that the bold letters denote vectors. The dipole magnetic moment amplitude is $\mu = M_s V_c$, where M_s [A/m] is the saturation magnetization of the material, and V_c [m^3] is the core volume of the particle. Using this energy formula, the magnetization M can be derived as follows (see Appendix A.1 for the detailed derivation):

$$M = \mu \rho \mathcal{L}(\xi) \tag{2.8}$$

This relation indicates that mean magnetization is dependent on the parameters of the MNPs, such as core volume V_c and saturation magnetization M_s, as shown in Figure 2.3.

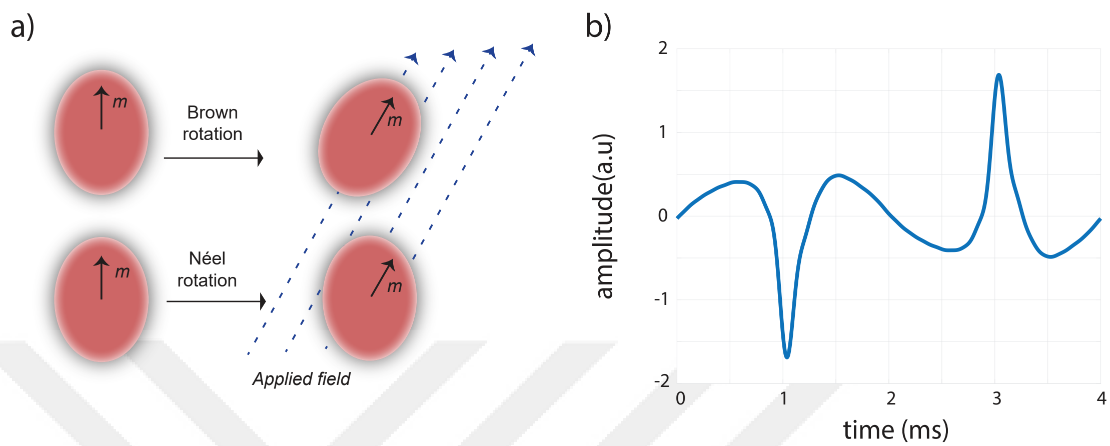

Figure 2.4: *(a) An illustration for Brown and Néel rotations. The vector* $\boldsymbol{m}$ *denotes the magnetic moment vector direction. While the particle physically rotates in the Brown process, the Néel process involves internal alignment. (b) An example MPS signal for Perimag MNPs at 15 mT, 250 Hz DF settings. The relaxation effect is apparent in the asymmetry of the signal, particularly at the alongated tail of the signal.*

2.3.2 Relaxation in MNPs

The adiabatic model assuming that the magnetization can simultaneously align with the field change, is not capable of explaining real-life magnetization dynamics. In reality, the MNPs experience some delay during alignment, which is called relaxation, due to the thermal fluctuations, energy barriers coming from the magnetic anisotropy, and viscous drag of the medium [26, 61, 62, 28]. To better understand the sources of this relaxation, this chapter will briefly describe the two rotation mechanisms governing the MNP alignment with the applied field: Néel and Brown rotations. Magnetization alignment of MNPs occurs through either Brown rotation or Néel rotation, or a combination of both. While the magnetic moment of the MNPs physically aligns with the applied field in Brown rotation, the alignment occurs internally without any physical rotation for Néel rotation, as illustrated in Figure 2.4(a). The viscous drag experienced by the particle affects the Brown rotation, and the zero-field Brown relaxation time constant is given as follows:

$$\tau_B = \frac{3V_h\eta}{k_BT} \tag{2.9}$$

Here, V_h is the hydrodynamic volume, η [mPa· s] is the viscosity.

The Néel rotation is affected by the energy barrier associated with the magnetic anisotropy effects. The magnetic anisotropy, stemming from magnetocrystalline and shape anisotropy, creates lower energy states at some specific directions for the magnetic moment vector. For the simplest case, the preferred direction, i.e., easy axis, is at two directions that are 180 ° apart. Other types of magnetic anisotropy include triaxial and cubic anisotropy. The zero-field Néel relaxation time constant is given as follows:

$$\tau_N = \frac{M_sV_c}{\gamma k_BT}\frac{1+\alpha^2}{2\alpha} \tag{2.10}$$

Here, α is the Gilbert damping parameter and γ is the gyromagnetic ratio. It is commonly stated that the dynamics are dominated by the fastest relaxation process, and the effective time constant (τ_{eff}) can be calculated as follows [63]:

$$\frac{1}{\tau_{eff}} = \frac{1}{\tau_N} + \frac{1}{\tau_B} \tag{2.11}$$

However, real-life dynamics deviate from this simplistic approach of the effective time constant. Firstly, the zero-field conditions are not typically applicable in MPI, where sinusoidal fields are commonly employed. Furthermore, empirical evidence demonstrates that the time constants τ_B and τ_N depend on the strength of the magnetic field [64], indicating that relying solely on zero-field time constants may not be helpful in practical scenarios. Regardless of the underlying mechanism, the relaxation effects on the MNP magnetization were previously modeled with a first-order Debye process using an exponential relaxation kernel as follows [62]:

$$s(t) = s_{adiabatic}(t) * r(t) \tag{2.12}$$

where the relaxation kernel $r(t)$ is defined as:

$$r(t) = \frac{1}{\tau} e^{\frac{-t}{\tau}} u(t) \tag{2.13}$$

Here, τ is the relaxation time constant and $u(t)$ is the unit step function. The following section provides detailed information on estimating τ without requiring any prior calibration.

Direct Estimation of the Relaxation Time Constant

A calibration-free method, called TAURUS (TAU estimation via Recovery of Underlying mirror Symmetry) [53, 25, 65, 24], has been proposed to estimate the τ value using the mirror symmetry between positive and negative half-cycles , which can be expressed as follows:

$$s_{half}(t) = s_{pos,ideal}(t) = -s_{neg,ideal}(-t) \tag{2.14}$$

Here, $s_{pos,ideal}(t)$ and $s_{neg,ideal}(t)$ are the ideal (i.e., without relaxation) half-cycle signals received from positive and negative scanning directions. The relaxation kernel blurs the received signal in the scanning direction, breaking the mirror symmetry between the positive and negative half-cycles, as shown in Fig. 2.5(a). The positive and negative half-cycle signals with the relaxation effect can be expressed as follows:

$$s_{pos}(t) = s_{pos,ideal}(t) * r(t) = s_{half}(t) * r(t) \tag{2.15}$$

$$s_{neg}(t) = s_{neg,ideal}(t) * r(t) = -s_{half}(-t) * r(t) \tag{2.16}$$

Taking the Fourier transformation, these relations can be rewritten as:

$$\mathscr{F}\{s_{pos}(t)\} = S_{pos}(f) = S_{half}(f)R(f) \tag{2.17}$$

$$\mathscr{F}\{s_{neg}(t)\} = S_{neg}(f) = -S_{half}(-f)R(f) \tag{2.18}$$

$$\mathscr{F}\{r(t)\} = R(f) = \frac{1}{(1 + i2\pi f\tau)} \tag{2.19}$$

Since the $s_{half}(t)$ is real-valued, $S_{half}(f)$ exhibits conjugate symmetry as follows:

$$S_{half}(-f) = S^{*}_{half}(f) \tag{2.20}$$

Mathematically manipulating the given equations, one can derive the following equation for τ:

$$\tau = \frac{S^{*}_{pos}(f) + S_{neg}(f)}{i2\pi f \left(S^{*}_{pos}(f) - S_{neg}(f)\right)} \tag{2.21}$$

One problem is that the measurement system can introduce an arbitrary time delay, making it difficult to distinguish the starting points of the positive and negative half-cycles. TAURUS jointly estimates this time delay and τ by selecting the parameters that minimize the mean square error (MSE) in mirror symmetry for the half-cycle signals deconvolved using the estimated τ.

2.3.3 Langevin Equations

If the timescales for the magnetic field change and MNP relaxation are comparable, the adiabatic model fails to capture the MNP dynamics. In such cases, the Langevin equations accounting for the relaxation effects can be employed. The Langevin equations are stochastic differential equations that incorporate deterministic and random components to describe the dynamics of a system [66, 61, 67, 68]. This section provides an overview of the derivation of the Langevin

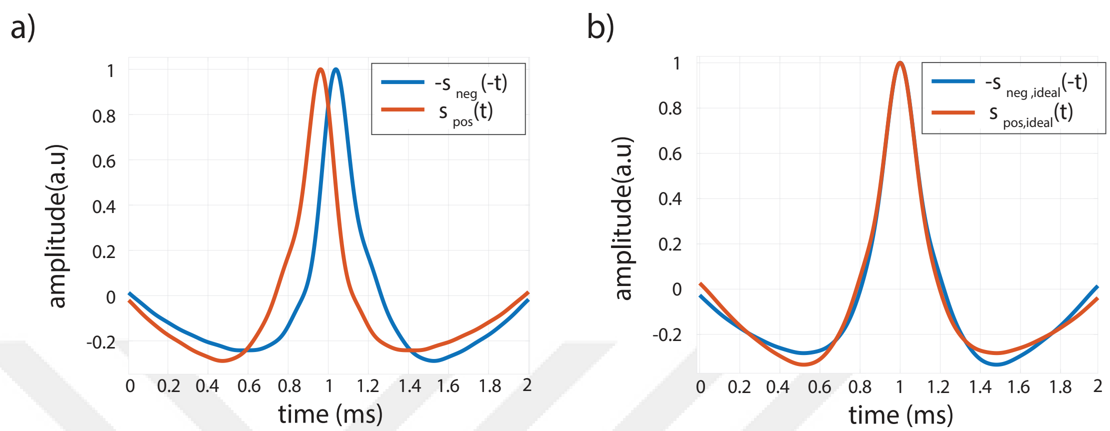

Figure 2.5: *(a) The mirrored negative half-cycle together with the positive half-cycle signal of Perimag MNPs measured with 15 mT, 250 Hz as DF settings. In the case of mirror symmetry, the positive half-cycle signal (red curve) and the flipped and negated negative half-cycle signal (blue curve) should overlap exactly. In reality, the mirror symmetry is broken due to the relaxation effects. Applying the TAURUS algorithm to this signal yields τ as 55.6 μs. (b) The ideal, i.e., without relaxation, negative and positive half-cycle signals were obtained through deconvolution using the relaxation kernel of the estimated τ as 55.6 μs. The mirror symmetry is recovered after deconvolution with the estimated τ.*

equations that describe pure Brown and pure Néel rotations. By solving these equations, we can obtain the magnetization response of a single MNP under a particular realization of stochastic forces. Repeating the solution for different realizations of stochastic forces is necessary to obtain the mean dynamics. This iterative process, known as Monte Carlo simulations, allows us to capture a range of possible outcomes and analyze the statistical behavior of the system.

The Langevin Equation for Brown Rotation

Considering non-interacting, magnetically isotropic MNPs modeled as dipoles, we have the following torque under the applied field:

$$\boldsymbol{T}_{mag} = \boldsymbol{\mu} \times \boldsymbol{B} \tag{2.22}$$

While rotating in a fluid, the particles also experience a viscous drag. Assuming that the MNPs have small Reynolds numbers (i.e. the ratio of inertial forces to the viscous forces within a fluid), the torque due to the viscous drag can be written as [26, 37, 69]:

$$\boldsymbol{T}_{vis} = -6\eta V_h \boldsymbol{\Omega} \tag{2.23}$$

where $\boldsymbol{\Omega}$ [1/s] is the angular velocity. Therefore, the overall torque can be written as:

$$\begin{aligned} \boldsymbol{T} &= \boldsymbol{T}_{mag} + \boldsymbol{T}_{vis} \\ &= \boldsymbol{\mu} \times \boldsymbol{B} - 6\eta V_h \boldsymbol{\Omega} \end{aligned} \tag{2.24}$$

From Newton's second law for rotation,

$$\boldsymbol{T} = I \frac{d\boldsymbol{\Omega}}{dt} \tag{2.25}$$

where I [kg·m^2] is the rotational inertia and $d\boldsymbol{\Omega}/dt$ is the angular acceleration. Under the assumption of a small Reynolds number, the inertial forces are negligible compared to viscous forces. Therefore, Equation (2.25) can be equated to zero, and the following equation can be obtained:

$$6\eta V_h \boldsymbol{\Omega} = \boldsymbol{\mu} \times \boldsymbol{B} \tag{2.26}$$

The angular velocity $\boldsymbol{\Omega}$ and the magnetic moment vector $\boldsymbol{m}$ are also dependent due to the fact only the perpendicular component of the angular velocity influences the rotational behavior of the magnetic moment vector [37, 70], yielding that:

$$\frac{d\boldsymbol{m}}{dt} = \boldsymbol{\Omega} \times \boldsymbol{m} \tag{2.27}$$

After some mathematical manipulations, the following equation can be derived (see Appendix A.2 for details):

$$\frac{d\boldsymbol{m}}{dt} = \frac{1}{2\tau_B}\left[(\boldsymbol{m}\times\boldsymbol{\xi})\times\boldsymbol{m}\right] \tag{2.28}$$

Here, $\boldsymbol{\xi} = \frac{M_s V_c \boldsymbol{B}}{k_B T}$. To incorporate stochasticity into Equation (A.12) due to the thermal effects resulting from random collisions between MNPs and fluid molecules, one can add a white noise torque that depends on the viscosity and the temperature as follows:

$$\frac{d\boldsymbol{m}}{dt} = \frac{1}{2\tau_B}\left[(\boldsymbol{m}\times\boldsymbol{\xi})\times\boldsymbol{m}\right] + \frac{\boldsymbol{Z}(t)\times\boldsymbol{m}}{\sqrt{\tau_B}} \tag{2.29}$$

Here, the following properties are assumed as a good approximation for the 3-D white noise $\boldsymbol{Z}(t)$ [26]:

$$\langle Z_i(t)\rangle = 0 \qquad \langle Z_i(t)Z_j(t+\Delta t)\rangle = \delta(i-j)\delta(\Delta t) \tag{2.30}$$

where δ is the Dirac delta function and i and j are any of the 3 coordinate dimension.

The Langevin Equation for Néel Rotation

The moving electrons have both spin magnetic moment $\boldsymbol{\mu_e}$ [Am^2] and angular momentum $\boldsymbol{L_e}$ [kg·m^2/s] due to having a charge and mass [27], which are related as follows:

$$\boldsymbol{\mu_e} = -\gamma\boldsymbol{L_e} \tag{2.31}$$

Here, γ [A·s/kg] is the gyromagnetic ratio for an electron. When the electrons are placed in an external magnetic field, they will try to align their magnetic moment with the applied field direction by spinning around the field axis. However, an electron also has a mass, and, thus, an angular momentum that opposes spinning around the field axis. This causes the precession of the electron around the field axis. The torque on each electron $\boldsymbol{T_e}$ is given by [27, 67]

$$\boldsymbol{T_e} = \boldsymbol{\mu_e} \times \boldsymbol{B} \tag{2.32}$$

Since the torque on the electron is equal to the time derivative of angular momentum, we have the following:

$$\begin{aligned} \frac{d\boldsymbol{L_e}}{dt} &= \boldsymbol{T_e} \\ -\frac{d\boldsymbol{\mu_e}}{\gamma dt} &= \boldsymbol{\mu_e} \times \boldsymbol{B} \end{aligned} \tag{2.33}$$

This is the gyromagnetic equation for an isolated electron. For MNPs, it is typically assumed that the dynamics of an individual electron can be used to describe the MNP magnetization dynamics [27], yielding that:

$$\frac{d\boldsymbol{m}}{dt} = -\gamma \boldsymbol{m} \times \boldsymbol{B} \tag{2.34}$$

This equation describes a precession around the field. To explain the alignment with the applied field, Landau and Lifshitz (LL) introduced a phenomenological term (i.e., based on observation) to the right-hand side of Equation (2.34) as follows:

$$\frac{d\boldsymbol{m}}{dt} = -\gamma' \boldsymbol{m} \times \boldsymbol{B} - \mathscr{K}(\boldsymbol{m} \times \boldsymbol{B}) \times \boldsymbol{m} \tag{2.35}$$

Here, γ' is the adjusted gyromagnetic ratio and $\mathscr{K}$ [s/kg·m] is the phenomenological damping coefficient. This equation, known as LL equation, represents a damped precessional motion. Later, Gilbert modified the gyromagnetic equation by introducing an effective damping field term [71]. He assumed that the alignment occurs due to the collisions of the electrons during precessional motion, which creates the following damping field:

$$\boldsymbol{B}_{damping} = -\frac{\alpha}{\gamma}\frac{d\boldsymbol{m}}{dt} \tag{2.36}$$

where α is the dimensionless damping factor. After including the damping field, the gyromagnetic equation becomes:

$$\begin{aligned}\frac{d\boldsymbol{m}}{dt} &= -\gamma \boldsymbol{m} \times (\boldsymbol{B} + \boldsymbol{B}_{damping}) \\ &= -\gamma \boldsymbol{m} \times \boldsymbol{B} + \alpha \boldsymbol{m} \times \frac{d\boldsymbol{m}}{dt}\end{aligned} \tag{2.37}$$

The resulting equation is Gilbert's equation implicit in $d\boldsymbol{m}/dt$. After some mathematical manipulations, the following relation can be obtained (see Appendix A.3):

$$2\tau_N \frac{d\boldsymbol{m}}{dt} = \frac{-V_c}{kT}\left[\frac{1}{\alpha}\boldsymbol{m} \times \boldsymbol{B} + \boldsymbol{m} \times (\boldsymbol{m} \times \boldsymbol{B})\right] \tag{2.38}$$

To introduce stochasticity into this equation and convert it to a Langevin equation, the magnetic field is modified as an effective field, incorporating both magnetic anisotropy and stochastic effects. The following is an example of an effective field after including uniaxial magnetic anisotropy and stochastic effects together with the applied DF [42]:

$$\boldsymbol{B}_{eff} = \boldsymbol{B_p} cos(2\pi f_d t) + \frac{2K}{M_s}(\boldsymbol{m} \cdot \boldsymbol{n})\boldsymbol{n} + \boldsymbol{h}(t) \tag{2.39}$$

where the first term is the applied DF as given in Equation (2.4), the second term is linked to the magnetic anisotropy energy, K [J/m^3] is the uniaxial magnetic anisotropy constant, and $\boldsymbol{n}$ is the unit vector describing easy axis direction. Lastly, $\boldsymbol{h}(t)$ is the time signal coming from a stochastic process, which can be selected as a white noise process for simplicity.

2.3.4 The Fokker-Planck Equations (FPE)

Section 2.3.3 provided an overview of the derivation of the Langevin functions that describe Brown and Néel rotations. To capture the magnetization dynamics of a specific MNP, the Langevin equations should be solved under different realizations of stochastic forces, and then the solutions should be averaged.

Alternative to this approach, the Fokker-Planck equations (FPE) can be utilized to describe the distribution of an ensemble of the magnetization vectors as time progresses. These are partial differential equations describing how the probability distribution of the variables belonging to an ensemble evolves over time. The derivation of the FPE equations requires defining the stochastic process. This section provides a brief overview of the derivation of generalized FPE for magnetic moment vector.

Firstly, the magnetization of each single MNP is denoted with a unit vector pointing to an arbitrary direction on a unit sphere [26]. Although the directions of the magnetization vectors change with the thermal fluctuations and magnetic field, the total number of these vectors remains constant. The distribution of these magnetization vectors can be described with a probability density function (PDF) depending on the spherical coordinates and time. Namely, $f(\theta, \phi, t)$ is the PDF of the magnetic moment vectors at azimuth angle θ, polar angle ϕ, and time t. Note that the function f does not depend on the radius r since all vectors are on the unit sphere surface. This function satisfies the following relation [26]:

$$\int f(\theta, \phi, t) dS = 1 \tag{2.40}$$

This relation shows that the total number of magnetic moment vectors is a conserved quantity. The change in this PDF leads to a surface current $\boldsymbol{J}(\theta, \phi, t)$. Using the differential form of the continuity equation,

$$\frac{\partial f(\theta, \phi, t)}{\partial t} = -\boldsymbol{\nabla} \cdot \boldsymbol{J}(\theta, \phi, t) \tag{2.41}$$

where the surface current $\boldsymbol{J}(\theta, \phi, t)$ depends on the magnetization change ($d\boldsymbol{m}/dt$) of each vector in the distribution. Furthermore, the thermal fluctuations induce magnetization variations, resembling a diffusion process. Therefore, an additional term proportional to the distribution density and a diffusion constant D was added [26]. In an intuitive sense, the diffusion term tries to make the distribution nearly uniform.

$$\frac{\partial f(\theta,\phi,t)}{\partial t} = -\nabla \cdot \left(\frac{d\boldsymbol{m}}{dt} - D\nabla\right) f(\theta,\phi,t) \tag{2.42}$$

Note that $d\boldsymbol{m}/dt$ can be replaced with the differential equation at zero temperature, i.e. without thermal fluctuations, which are Eqs. (A.12) and (A.20) for Brown rotation and Néel rotation, respectively. The expected value of the magnetization vector gives us the mean magnetization dynamics of the MNP, calculated as follows:

$$\langle \boldsymbol{m} \rangle = \int \boldsymbol{m} f(\theta,\phi,t) d\boldsymbol{S} \tag{2.43}$$

The Fokker-Planck Equations for Brown rotation

The following equation can be derived for FPE of Brown rotation with $x = \cos\theta$ (see Appendix A.4 for details):

$$2\tau_B \frac{\partial f(\theta,t)}{\partial t} = \frac{\partial}{\partial x}\left[(1-x^2)\left(\frac{\partial f(\theta,t)}{\partial x} - \xi(t) f(\theta,t)\right)\right] \tag{2.44}$$

This resulting partial differential equation is FPE for Brown rotation of MNPs with uniaxial symmetry. The extension of $f(\theta,t)$ to Legendre polynomials [61], as shown below, is a commonly used technique to solve Equation (2.44):

$$f(\theta,t) = \sum_{n=0}^{\infty} a_n(t) P_n(cos\theta) \tag{2.45}$$

Here, P_n's are Legendre polynomials which form a complete and orthogonal set of polynomials possessing unique properties. The coefficients a_n are associated with their respective polynomials. Equivalently, we have:

$$f(x,t) = \sum_{n=0}^{\infty} a_n(t) P_n(x) \tag{2.46}$$

After a lengthy derivation (see Appendix A.5 for details), the following relation between ODE of coefficients for P_m can be obtained:

$$\frac{\mathrm{d}a_m}{\mathrm{d}t} = \frac{m(m+1)}{2\tau_B}\left[-a_m + \xi(t)\left[\frac{a_{m-1}}{2m-1} - \frac{a_{m+1}}{2m+3}\right]\right] \tag{2.47}$$

To solve the above system of ODEs, one option is to truncate the expansion and then numerically solve. Alternatively, the ODEs can be solved using techniques such as finite element methods [72], continued fraction approximation, or the eigenvalues approach [73]. For instance, by utilizing $f(x,t)$ being a PDF, $P_0(x) = 1$, and the orthogonality property, $a_0(t)$ can be calculated as follows:

$$\begin{aligned} \int_{-1}^{1} f(x,t)\mathrm{d}x &= 1 \\ \int_{-1}^{1} P_0(x) \sum_{n=0}^{\infty} a_n(t) P_n(x) \mathrm{d}x &= 1 \\ a_0(t)\frac{2}{2.0+1} &= 1 \\ a_0(t) &= \frac{1}{2} \end{aligned} \tag{2.48}$$

Finally, the relation between the mean magnetization and the series coefficients is derived by utilizing the orthogonality property and $P_1(x) = x$ as follows:

$$\begin{aligned} \langle x(t) \rangle &= \int_{-1}^{1} x(t) f(x,t)\mathrm{d}x \\ &= \int_{-1}^{1} P_1(x) \sum_{n=0}^{\infty} a_n(t) P_n(x)\mathrm{d}x \\ &= a_1(t)\frac{2}{2.1+1} = a_1(t)\frac{2}{3} \end{aligned} \tag{2.49}$$

The Fokker-Planck Equations for Néel rotation

Unlike Brown FPE given in Equation 2.44, FPE for Néel rotation assuming uniaxial symmetry includes an anisotropy term as follows [61]:

$$2\tau_N \frac{\partial f(\theta,t)}{\partial t} = \frac{\partial}{\partial x}\left[(1-x^2)\left(\frac{\partial f(\theta,t)}{\partial x} - \xi(t) f(\theta,t) + \frac{2KV_c}{k_B T} f(\theta,t)\right)\right] \tag{2.50}$$

This FPE for Néel rotation assumes uniaxial magnetic anisotropy where the easy axis is aligned with the applied magnetic field direction. Similar to solving Brown FPE, $f(\theta,t)$ will be expanded to Legendre polynomials as given in Equation (2.45). Then, the Legendre polynomials have the following coefficients:

$$\begin{aligned}\frac{\mathrm{d}a_m}{\mathrm{d}t} = \frac{m(m+1)}{2\tau_B}\Bigg[- a_m + \xi(t)\left[\frac{a_{m-1}}{2m-1} - \frac{a_{m+1}}{2m+3}\right] + \frac{2KV_c}{k_B T}\Bigg[\frac{(m-1)a_{m-2}}{(2m-3)(2m-1)} \\ + \frac{m a_m}{(2m-1)(2m+1)} - \frac{(m+1)a_m}{(2m+1)(2m+3)} - \frac{(m+2)a_{m+2}}{(2m+3)(2m+5)}\Bigg]\Bigg]\end{aligned} \tag{2.51}$$

Similar to Brown FPE, $a_0 = 1/2$ is given by the normalization requirement of PDF, as calculated in Equation (2.48). Furthermore, the mean magnetization can be calculated with $\langle x(t)\rangle = 2a_1(t)/3$, as derived in Equation (2.49).

The Fokker-Planck Equations for Coupled Brown-Néel rotation

FPE for coupled Brown-Néel rotation was derived from coupled Langevin equations in [47], allowing arbitrary direction for the applied field, easy axis, and magnetic moment vector. The coupled Langevin equations are given in terms of two unit vectors representing the magnetic moment ($\boldsymbol{m}$) and easy axis direction ($\boldsymbol{n}$) as follows [47]:

$$\begin{aligned}\frac{d\boldsymbol{n}}{dt} &= \frac{KV_c}{3\eta V_H}(\boldsymbol{n}\cdot\boldsymbol{m})\left[(\boldsymbol{n}\times\boldsymbol{m})\times\boldsymbol{n}\right] + \frac{1}{\sqrt{\tau_B}}\boldsymbol{Y}(t)\times\boldsymbol{n} \\ \frac{\boldsymbol{dm}}{dt} &= \frac{1}{2\tau_N}\frac{M_s V_c}{\alpha k_B T}\Bigg[\left[\boldsymbol{m}\times\left(\boldsymbol{B} + \frac{2K}{M_s}(\boldsymbol{m}\cdot\boldsymbol{n})\boldsymbol{n}\right)\right] \\ &\quad + \left[\boldsymbol{m}\times\left(\boldsymbol{B} + \frac{2K}{M_s}(\boldsymbol{m}\cdot\boldsymbol{n})\boldsymbol{n}\right)\right]\times\boldsymbol{m}\Bigg] \\ &\quad + \frac{1}{\sqrt{(1+\alpha^2)\tau_N}}\left[\boldsymbol{m}\times\boldsymbol{X}(t) + (\boldsymbol{m}\times\boldsymbol{X}(t))\times\boldsymbol{m}\right]\end{aligned} \tag{2.52}$$

These equations describe the time evolvement of the magnetic moment direction and easy axis direction. The coupling between the equations implies that these evolvements are dependent on each other. Here, $\boldsymbol{X}$ and $\boldsymbol{Y}$ are the stochastic processes with the following statistics:

$$
\begin{aligned}
&\langle X_i(t)X_j(t+\varDelta t)\rangle = \delta(i-j)\delta(\varDelta t)\\
&\langle Y_i(t)Y_j(t+\varDelta t)\rangle = \delta(i-j)\delta(\varDelta t)\\
&\langle X_i(t)] = \langle Y_i(t)\rangle = \langle X_i(t)Y_j(t+\varDelta t)\rangle = 0
\end{aligned}
$$

Two spherical coordinate systems are defined for $\boldsymbol{n}$ as (ρ, θ, ϕ) and for $\boldsymbol{m}$ as (r, ϑ, φ). The unit vectors $\boldsymbol{n}$ and $\boldsymbol{m}$ are expressed as follows

$$\boldsymbol{n} = N_\rho \boldsymbol{e_\rho} + N_\theta \boldsymbol{e_\theta} + N_\phi \boldsymbol{e_\phi} \tag{2.53}$$

$$\boldsymbol{m} = E_\rho \boldsymbol{e_r} + N_\vartheta \boldsymbol{e_\vartheta} + N_\varphi \boldsymbol{e_\varphi} \tag{2.54}$$

where $\boldsymbol{e}$'s are the basis vector for the spherical coordinates. Note that $\boldsymbol{n} = \boldsymbol{e_\rho}$ and $\boldsymbol{m} = \boldsymbol{e_r}$. The following normalized potentials are introduced for simplification purposes:

$$\mathscr{N}_K = \frac{KV_c}{k_B T} N_\rho^2 = \frac{KV_c}{k_B T} E_r^2 \tag{2.55}$$

$$\mathscr{N}_B = \frac{M_s V_c}{k_B T} B_\rho \tag{2.56}$$

Defining the PDF $f(\vartheta, \varphi, \theta, \phi)$ for the joint distribution of magnetic moment and easy axis vector, the following FPE is derived after a lengthy derivation (see [47] for details):

$$
\begin{aligned}
\frac{\partial f}{\partial t} &= \frac{1}{2\tau_B}\left[\frac{1}{\sin\vartheta}\frac{\partial}{\partial\vartheta}\left(\sin\vartheta\frac{\partial f}{\partial\vartheta}\right)+\frac{1}{\sin^2\vartheta}\frac{\partial^2 f}{\partial\varphi^2}\right] \\
&- \frac{1}{2\tau_N}\left[\frac{1}{\sin\theta}\frac{\partial}{\partial\theta}\left(\sin\theta\frac{\partial\mathscr{N}_K}{\partial\theta}\right)+\frac{1}{\sin^2\theta}\frac{\partial^2\mathscr{N}_K}{\partial\phi^2}\right] \\
&- \frac{1}{2\tau_B}\left[\frac{1}{\sin\vartheta}\frac{\partial}{\partial\vartheta}\left(\sin\vartheta\frac{\partial\mathscr{N}_K}{\partial\vartheta}\right)+\frac{1}{\sin^2\vartheta}\frac{\partial^2\mathscr{N}_K}{\partial\varphi^2}\right] \\
&+ \frac{1}{2\tau_N}\left[\frac{1}{\sin\theta}\frac{\partial}{\partial\theta}\left(\sin\theta\frac{\partial f}{\partial\theta}\right)+\frac{1}{\sin^2\theta}\frac{\partial^2 f}{\partial\phi^2}\right] \\
&- \frac{1}{2\tau_N}\left[\frac{1}{\sin\theta}\frac{\partial}{\partial\theta}\left(\sin\theta\frac{\partial\mathscr{N}_B}{\partial\theta}\right)+\frac{1}{\sin^2\theta}\frac{\partial^2\mathscr{N}_B}{\partial\phi^2}\right] \\
&- \frac{1}{2\tau_N}\left[\frac{\partial\mathscr{N}_B}{\partial\theta}\frac{\partial f}{\partial\theta}+\frac{1}{\sin^2\theta}\frac{\partial\mathscr{N}_B}{\partial\phi}\frac{\partial f}{\partial\phi}\right] \\
&- \frac{1}{2\tau_B}\left[\frac{\partial\mathscr{N}_K}{\partial\vartheta}\frac{\partial f}{\partial\vartheta}+\frac{1}{\sin^2\vartheta}\frac{\partial\mathscr{N}_K}{\partial\varphi}\frac{\partial f}{\partial\varphi}\right]-\frac{1}{2\tau_N}\left[\frac{\partial\mathscr{N}_K}{\partial\theta}\frac{\partial f}{\partial\theta}+\frac{1}{\sin^2\theta}\frac{\partial\mathscr{N}_K}{\partial\phi}\frac{\partial f}{\partial\phi}\right] \\
&+ \frac{1}{2\tau_N}\frac{1}{\alpha}\frac{1}{\sin\theta}\left[\frac{\partial\mathscr{N}_B}{\partial\phi}\frac{\partial f}{\partial\theta}-\frac{\partial\mathscr{N}_B}{\partial\theta}\frac{\partial f}{\partial\phi}\right]+\frac{1}{2\tau_N}\frac{1}{\alpha}\frac{1}{\sin\theta}\left[\frac{\partial\mathscr{N}_K}{\partial\phi}\frac{\partial f}{\partial\theta}-\frac{\partial\mathscr{N}_K}{\partial\theta}\frac{\partial f}{\partial\phi}\right]
\end{aligned} \tag{2.57}
$$

Similar to the solution of Brown and Néel FPE, the PDF $f(\vartheta,\varphi,\theta,\phi)$ was expanded with series expansion using spherical harmonics as

$$
f(\vartheta,\varphi,\theta,\phi)=\sum_{l=0}^{\infty}\sum_{m=-l}^{l}\sum_{r=0}^{\infty}\sum_{q=-r}^{r} D_{l,r}^{m,q}P_l^m(\vartheta)e^{im\varphi}P_r^q(\theta)e^{iq\phi} \tag{2.58}
$$

where $P_a^b(\cdot)$ are the Legendre polynomials and $D_{l,r}^{m,q}$ are the expansion coefficients. Inserting Equation (2.58) into Equation (2.57) and after mathematical manipulations (see [47] for details), a system of ODEs gives the solution as

$$
\frac{dD_{l,r}^{m,q}}{dt}=\sum_{\Delta l=-2}^{2}\sum_{\Delta m=-2}^{2}\sum_{\Delta r=-2}^{2}\sum_{\Delta q=-2}^{2} c_{\Delta l,\Delta m}(l,m)g_{\Delta r,\Delta q}(r,q)D_{(l-\Delta l),(r-\Delta r)}^{(m-\Delta m),(q-\Delta q)} \tag{2.59}
$$

where $c_{\Delta l,\Delta m}(l,m)g_{\Delta r,\Delta q}(r,q)$ values are derived and given in Appendix C and D of [47]. In case of uniaxial symmetry $(m,q=0)$, Equation (2.59) simplifies to

$$\frac{dD_{l,r}^{0,0}}{dt} = \sum_{\Delta l=-2}^{2} \sum_{\Delta r=-2}^{2} c_{\Delta l,0}(l,0) g_{\Delta r,0}(r,0) D_{(l-\Delta l),(r-\Delta r)}^{0,0} \tag{2.60}$$

The related coefficients $c_{\Delta l,0}(l,0)g_{\Delta r,0}(r,0)$ are given in Appendix E of [47].

Chapter 3

MNP Signal Prediction at Untested Viscosity Levels

This chapter is partly based on the following publication:

A. Alpman, M. Utkur, E.U. Saritas. "MNP Characterization and Signal Prediction using a Model-Based Dictionary", Proc of the 11th International Workshop on Magnetic Particle Imaging, Virtual Conference, p. 2203017, March 2022. DOI: 10.18416/IJMPI.2022.2203017

3.1 Theory

3.1.1 Coupled Brown-Néel Rotation Model

To simulate the magnetization dynamics of MNPs, we utilized the coupled Brown–Néel rotation model [47], as described in Section 2.3.4, This model assumes single-domain, noninteracting, uniaxially symmetric particles with uniaxial magnetic anisotropy. Although there exist computationally simpler magnetization models such as the Langevin, pure Brown, and pure Néel models, the coupled model captures the magnetization dynamics more comprehensively than others.

Figure 3.1 compares the simulated MNP signals from different models for two different viscosity levels of 0.89 mPa·s and 15.33 mPa·s, at DF frequencies of 250 Hz and 1 kHz at 10 mT amplitude. The MNP parameters were chosen according to the values in the literature as determined via magnetic characterization [74]. Here, the Néel rotation results are shown for two different scenarios: (1) the aligned Néel model, where the easy axis (i.e., the easiest direction to magnetize the material) and applied field were assumed to be aligned [40], and (2) the Brown–Néel model at extremely high viscosity (100 Pa·s) to block Brown rotation, where the projection of the easy axis onto the applied field direction was assumed to have a zero mean [47]. These two Néel models yield similar relaxation delays, albeit with different signal amplitudes due to the differences in the initial alignment of the easy axis. In addition, the Langevin model assumes that the relaxation effects are negligible and the particles are at equilibrium. Because the two Néel models and the Langevin model do not incorporate the effects of viscosity on magnetization, their signals remain unchanged with viscosity. While the pure Brown model incorporates viscosity effects, its signal shows a low amplitude and noticeable relaxation delay due to slow alignment with the field, especially at higher frequencies. In contrast, the coupled Brown–Néel model shows reduced relaxation delay when compared to both the Néel models and the Brown model, while capturing the effects of viscosity. Consequently, for a realistic MNP simulation, the coupled Brown–Néel model offers a distinct advantage by more comprehensively capturing the magnetization dynamics of the MNPs.

3.1.2 Dictionary Formation

In this work, the MNP signals simulated using the coupled Brown–Néel model were used to form a dictionary matrix, with each column containing the odd harmonics in the Fourier transform of the simulated signal for MNPs with different magnetic parameters. As the MNP signals change with applied DF and viscosity, we built separate dictionaries for each DF and viscosity pair. Namely, $\boldsymbol{A}_{(\boldsymbol{k},\boldsymbol{j})} \in$

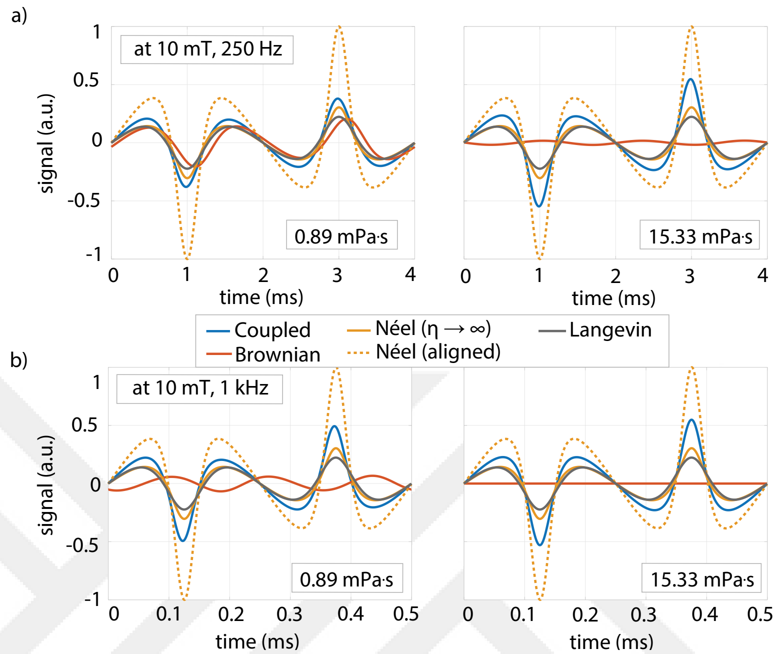

Figure 3.1: Simulated signals for a single MNP having 20 nm as core diameter, 60 nm as hydrodynamic diameter, and 6 kJ/m^3 as magnetic anisotropy constant. The magnetization responses were simulated and converted to signals at 0.89 mPa·s and 15.33 mPa·s for (a) 10 mT, 250 Hz, and (b) 10 mT, 1 kHz. The MNP signals were calculated by taking the time derivative of the magnetization responses and then filtering out the first harmonic. Signal amplitudes were normalized such that the maximum amplitude would be one within each DF setting.

$\mathbb{R}^{M_k \times N}$ is the dictionary matrix constructed in the frequency domain for the k^{th} drive field DF$_k$ and the j^{th} viscosity η_j. Here, N is the number of simulated particles, and M_k is the number of selected harmonics for DF$_k$. The constructed dictionaries were then utilized for linear inverse problem formulation to express the measured MNP signal as a weighted linear combination of the dictionary columns, as described below.

3.1.3 Incorporating Non-Model Based Dynamics

Solving a linear system of equations constructed with model-based dictionaries and measured MNP signals enables the weight estimation of the dictionary elements. However, solving directly for the dictionary weights is error-prone due to the non-model based dynamics, which are two-fold: First, the system response of the measurement setup alters the measured signals. If this effect is not accounted for, the estimated dictionary weights will need to compensate for the system response. However, this compensation may not work well for measurements performed at multiple frequencies. Second, the employed magnetization model may not fully account for real-life MNP dynamics, causing the dictionary weights to include arbitrary particles to explain the measured MNP dynamics.

Here, we incorporate these non-model based dynamics into the problem via a linear and time-invariant (LTI) system approach as shown in Fig. 3.2.a. Accordingly, the measured MNP signal is expressed as the multiplication of the MNP signal spanned by the dictionary and the transfer function of an LTI system:

$$H_k(f)\,\tilde{S}_{k,j}(f) = S_{k,j}(f) \tag{3.1}$$

Here, H_k is the transfer function of the LTI system representing non-model based dynamics for DF_k. $S_{k,j}$ and $\tilde{S}_{k,j}$ are the measured signal and the signal spanned by the dictonary at DF_k and η_j, respectively. We assume that the transfer function does not depend on the sample viscosity but may change with the drive field settings for a measured MNP sample. The non-model based dynamics were effected by the DF settings (i.e. DF frequency and amplitude), as both the impedances in the measurement setup and the dipolar interactions depend on these parameters [29, 30]. Additionally, the non-model based dynamics change depending on the MNP sample due to the changing dipolar interactions and magnetic anisotropy type. The dipolar interactions are affected by whether the MNPs are multi-core or single-core [75, 76], as well factors such as interparticle distances [29, 30, 31, 32, 33, 34, 77], which may vary among distinct MNP sample. Besides dipolar interaction, the magnetic anisotropy type changes for different MNP samples [78].

3.1.4 Simultaneous Estimation of Dictionary Weights and Transfer Functions

We propose finding the dictionary weights that, together with the transfer functions, explain the measured MNP signals. Accordingly, the problem can be formulated as follows:

$$\begin{aligned} \min_{\boldsymbol{x}\in\mathbb{R}^N,\{\boldsymbol{H_k}:\forall k\in D\}} & \sum_{k\in D}\sum_{j\in V} \left\| \boldsymbol{H_k} \boldsymbol{A_{(k,j)}} \boldsymbol{x} - \boldsymbol{s_{(k,j)}} \right\|_2^2 \\ \text{s.t.} \quad & \boldsymbol{x} \geq 0 \end{aligned} \tag{3.2}$$

Here, $\boldsymbol{s_{(k,j)}} \in \mathbb{R}^{M_k\times 1}$ is the measurement vector at DF_k and η_j, $\boldsymbol{H_k} \in \mathbb{R}^{M_k\times M_k}$ is a diagonal matrix with the diagonal entries containing the transfer function values at the harmonics, and $\boldsymbol{x} \in \mathbb{R}^{N\times 1}$ is the dictionary weights to be estimated. Lastly, D is the set of all DF indices, and V is the set of all viscosity indices.

This problem can be solved by adopting an alternating minimization approach in two steps: *transfer function update* and *weight update*. The proposed algorithm, summarized in Fig. 3.2.b, is initialized with a normalized uniform weight vector. A harmonic selection is employed for MPS measurements, subject to a signal-to-interference ratio thresholding. Then, the algorithm alternately optimizes either the weight vector or the transfer functions, while keeping the other fixed, for a predetermined maximum number of iterations. The two optimization steps are described in detail below.

3.1.5 Transfer Function Update

Keeping the weight vector fixed, the optimization problem becomes:

$$\min_{\{\boldsymbol{H_k}:\forall k\in D\}} \sum_{k\in D}\sum_{j\in V} \left\| \boldsymbol{H_k}\, \tilde{\boldsymbol{s}}_{\boldsymbol{(k,j)}} - \boldsymbol{s_{(k,j)}} \right\|_2^2 \tag{3.3}$$

where

$$\tilde{\boldsymbol{s}}_{\boldsymbol{(k,j)}} = \boldsymbol{A_{(k,j)}} \boldsymbol{x} \tag{3.4}$$

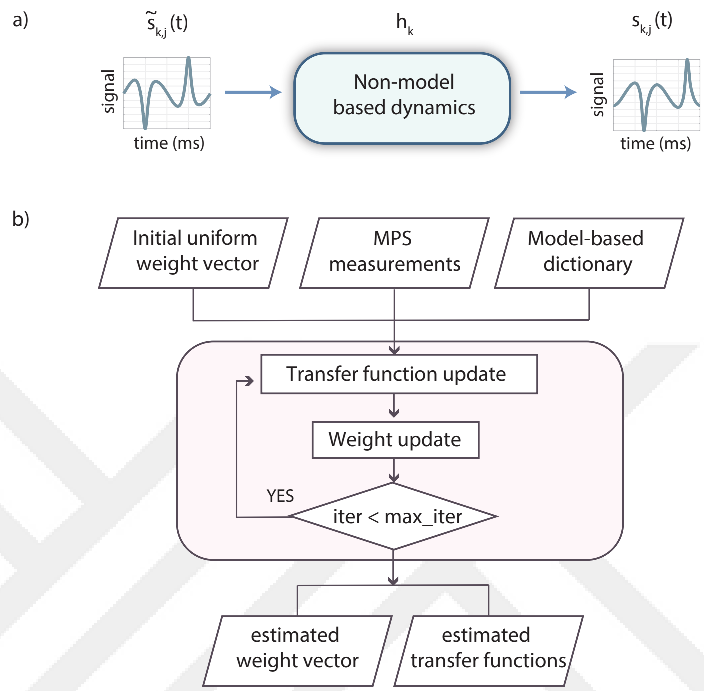

Figure 3.2: (a) The measured MNP signal ($s_{k,j}$) is modeled as the output of an LTI system (h_k), representing the non-model based dynamics at DF$_k$, given the spanned signal as input ($\tilde{s}_{k,j}$). (b) Flowchart of the proposed algorithm alternating between the transfer function update and weight update until the maximum iteration is reached. The proposed algorithm jointly estimates the weight vector and the transfer functions, given a uniform initial weight vector, MPS measurement, and the model-based dictionaries as input.

Here, $\tilde{\boldsymbol{s}}_{(\boldsymbol{k},\boldsymbol{j})} \in \mathbb{R}^{M_k \times 1}$ is fixed for a fixed $\boldsymbol{x}$. Note that this problem is now separable in DF indices. Hence, the optimization for the k^{th} drive field DF$_k$ can be performed independently from others as follows:

$$\hat{\boldsymbol{H}}_{\boldsymbol{k}} = \underset{\boldsymbol{H}_{\boldsymbol{k}} \in \mathbb{R}^{M_k \times M_k}}{\operatorname{argmin}} \sum_{j \in V} \left\| \boldsymbol{H}_{\boldsymbol{k}} \, \tilde{\boldsymbol{s}}_{(\boldsymbol{k},\boldsymbol{j})} - \boldsymbol{s}_{(\boldsymbol{k},\boldsymbol{j})} \right\|_2^2 \tag{3.5}$$

where $\hat{\boldsymbol{H}}_{\boldsymbol{k}}$ is the estimated transfer function. Because $\boldsymbol{H}_{\boldsymbol{k}}$ is a diagonal matrix, this problem is also separable in harmonic indices. For the m^{th} harmonic, the problem can be expressed as

$$\min_{H_k(mf_k)} \sum_{j \in V} \left\| H_k(mf_k) \, \tilde{S}_{k,j}(mf_k) - S_{k,j}(mf_k) \right\|_2^2 \tag{3.6}$$

where f_k is the fundamental frequency for DF_k. Using least square solution via Moore-Penrose pseudoinverse, the scalar $\hat{H}_k(mf_k)$ can be found as

$$\hat{H}_k(mf_k) = \frac{\sum_{j \in V} \tilde{S}^*_{k,j}(mf_k)\, S_{k,j}(mf_k)}{\sum_{j \in V} \left(\tilde{S}_{k,j}(mf_k)\right)^2} \tag{3.7}$$

where superscript $*$ denotes complex conjugation. After solving (3.7) for each drive field setting DF_k and harmonic m, the transfer function update step is completed.

3.1.6 Weight Update

Keeping the transfer functions fixed, the optimization problem becomes a standard nonnegative least square (NNLS) problem as follows:

$$\begin{aligned} \hat{\boldsymbol{x}} = \underset{\boldsymbol{x} \in \mathbb{R}^N}{\operatorname{argmin}} \sum_{k \in D} \sum_{j \in V} \left\| \hat{\boldsymbol{H}}_{\boldsymbol{k}} \boldsymbol{A}_{(\boldsymbol{k},\boldsymbol{j})} \boldsymbol{x} - \boldsymbol{s}_{(\boldsymbol{k},\boldsymbol{j})} \right\|_2^2 \\ \text{s.t.} \quad \boldsymbol{x} \geq 0 \end{aligned} \tag{3.8}$$

This problem can be solved by vertically concatenating the matrices $\hat{\boldsymbol{H}}_{\boldsymbol{k}} \boldsymbol{A}_{(\boldsymbol{k},\boldsymbol{j})}$ for different drive field settings and viscosities, with the real and imaginary parts separated and concatenated. Then, the problem can be expressed as:

$$\begin{aligned} \hat{\boldsymbol{x}} = \underset{\boldsymbol{x} \in \mathbb{R}^N}{\operatorname{argmin}} \left\| \bar{\boldsymbol{A}} \boldsymbol{x} - \bar{\boldsymbol{s}} \right\|_2^2 \\ \text{s.t.} \quad \boldsymbol{x} \geq 0 \end{aligned} \tag{3.9}$$

Here, $\bar{\boldsymbol{A}} \in \mathbb{R}^{2JM \times N}$ is the concatenated matrix, and $\bar{\boldsymbol{s}} \in \mathbb{R}^{2JM \times 1}$ is the concatenated measurement vector, with $M = \sum_{k \in D} M_k$ corresponding to the total number selected harmonics across all DF settings and J is the cardinality of set V (i.e., the total number of different viscosities considered).

Note that at the end of the transfer function and weight update stages, one can obtain infinitely many solution pairs $(\hat{\boldsymbol{x}}, \hat{\boldsymbol{H}}_k)$, due to the fact that an arbitrary scaling, i.e., $(k\hat{\boldsymbol{x}}, \hat{\boldsymbol{H}}_k/k)$ for some arbitrary constant k yields the same minimization error. However, such a scaling factor does not affect the signal fitting or signal prediction stages, since $\hat{\boldsymbol{x}}$ and $\hat{\boldsymbol{H}}_k$ are multiplied during those stages, as explained below.

3.1.7 MNP Signal Fitting

Using the estimated weight vector $\hat{\boldsymbol{x}}$, the signals spanned by the dictionary (i.e., excluding the non-model based dynamics) were calculated as follows:

$$\tilde{\boldsymbol{s}}_{(\boldsymbol{k},\boldsymbol{j})} = \boldsymbol{A}_{(\boldsymbol{k},\boldsymbol{j})}\hat{\boldsymbol{x}} \tag{3.10}$$

where $\tilde{\boldsymbol{s}}_{(\boldsymbol{k},\boldsymbol{j})} \in \mathbb{R}^{M_k \times 1}$ includes the harmonics of the signal spanned by the dictionary. Incorporating the estimated transfer functions $\hat{\boldsymbol{H}}_{\boldsymbol{k}}$, we can obtain the fit for the measured signals as follows:

$$\hat{\boldsymbol{s}}_{(\boldsymbol{k},\boldsymbol{j})} = \hat{\boldsymbol{H}}_{\boldsymbol{k}}\tilde{\boldsymbol{s}}_{(\boldsymbol{k},\boldsymbol{j})} = \hat{\boldsymbol{H}}_{\boldsymbol{k}}\boldsymbol{A}_{(\boldsymbol{k},\boldsymbol{j})}\hat{\boldsymbol{x}} \tag{3.11}$$

Here, $\hat{\boldsymbol{s}}_{(\boldsymbol{k},\boldsymbol{j})} \in \mathbb{R}^{M_k \times 1}$ contains the harmonics of the fitted signals.

3.1.8 MNP Signal Prediction

The goal of MNP signal prediction is to predict the signals for an untested setting, such as a viscosity level that has not been included in the measurements (i.e., not included when estimating $(\hat{\boldsymbol{x}}, \hat{\boldsymbol{H}}_k)$). For this purpose, we propose forming a new dictionary by simulating the MNP signals at the new viscosity level using the coupled Brown-Néel model. Then, the predicted signals spanned by the new dictionary can be calculated as:

$$\tilde{\boldsymbol{s}}_{(\boldsymbol{k},\boldsymbol{e})} = \boldsymbol{A}_{(\boldsymbol{k},\boldsymbol{e})}\hat{\boldsymbol{x}} \tag{3.12}$$

Incorporating the transfer functions, the final predicted MNP signals at the untested viscosity level can be expressed as:

$$\hat{\boldsymbol{s}}_{(\boldsymbol{k},\boldsymbol{e})} = \hat{\boldsymbol{H}}_{\boldsymbol{k}}\boldsymbol{A}_{(\boldsymbol{k},\boldsymbol{e})}\hat{\boldsymbol{x}} \tag{3.13}$$

Here, $\boldsymbol{A}_{(\boldsymbol{k},\boldsymbol{e})} \in \mathbb{R}^{M_k \times N}$ is the constructed new dictionary at DF$_k$ at the untested viscosity, where the index '$\boldsymbol{e}$' indicates that this viscosity level was 'excluded' from consideration when estimating $(\hat{\boldsymbol{x}}, \hat{\boldsymbol{H}}_k)$. Lastly, $\tilde{\boldsymbol{s}}_{(\boldsymbol{k},\boldsymbol{e})}, \hat{\boldsymbol{s}}_{(\boldsymbol{k},\boldsymbol{e})} \in \mathbb{R}^{M_k \times 1}$ contain the harmonics of the spanned and predicted signals.

3.2 Methods

3.2.1 Magnetization Simulations for Dictionary Formation

For dictionary formation, magnetization simulations were performed using the coupled Brown–Néel rotation model [47] for MNPs with different magnetic core diameter (d_c), surface coating diameter (d_s), and uniaxial magnetic anisotropy constant (K). The ranges for the simulated magnetic parameters are given in Table 3.1. The hydrodynamic diameter (d_h) was assumed to be the sum of the surface coating diameter and magnetic core diameter (i.e., $d_h = d_s + d_c$). Saturation magnetization (M_s) and temperature were assumed to be 360 kA/m [74], and 298.5 K, respectively. Gilbert damping constant and gyromagnetic ratio were taken as 0.1 and 1.75×10^{11} rad/(s·T), respectively [40].

At a given DF setting DF$_k$ and viscosity level η_j, the magnetization response for a given set of magnetic parameters was simulated by solving the ordinary differential equations (ODEs) given in Appendix E of [47], via the built-in variable-step variable-order solver *ode15s* of MATLAB. The initial conditions for ODE were assigned such that the particles have zero average magnetization. The magnetization response was simulated for three DF periods, with the first two periods later discarded to avoid the transient state. The resulting magnetization response was then sampled at a rate of 2 MS/s. Next, the corresponding MNP signal was computed by taking the numerical derivative of the simulated magnetization response with respect to time, multiplied by the respective core volumes. The spherical harmonics series expansion was truncated after the first 60 coefficients. Finally, the Fourier transform of this signal was inserted into the corresponding column of the dictionary matrix $\boldsymbol{A}_{(\boldsymbol{k},\boldsymbol{j})}$.

In total, 4680 different MNPs were simulated under 6 different DF settings and 6 different viscosity levels, resulting in 168480 distinct simulations (see Table 3.1). The DF settings consisted of two different DF amplitudes (B_p) of 10 mT and 15 mT, and three different DF frequencies (f_d) of 250 Hz, 1 kHz, and 2 kHz. These relatively low DF frequencies were selected as they were previously shown to have a high sensitivity to detect changes in viscosity [24, 25]. The viscosity levels ranged between 0.89-15.33 mPa $\cdot$ s.

Table 3.1: Parameters for Magnetization Simulations

MNP Parameters	d_c (nm)	$\{10, 11, 12, ..., 30\}$
	d_s (nm)	$\{15, 20, 25, ..., 100\}$
	K (kJ/m^3)	$\{1, 2, 3, ..., 10\}$
DF Settings	f_d (Hz)	$\{250, 1000, 2000\}$
	B_p (mT)	$\{10, 15\}$
Viscosity	η (mPa $\cdot$ s)	{0.89, 1.45, 2.08, 3.32, 8.31, 15.33}

3.2.2 Validation on Synthetic MNP Signals

For the case of experimental measurements, ground-truth weight vectors and transfer functions are generally not available. Therefore, to validate the performance of the proposed algorithm, we first generated synthetic MNP signals for known parameters, and then utilized the proposed algorithm to estimate the underlying weight vector and transfer functions. For this validation study, first a weight vector consisting of a single type of MNP was assigned. Then, synthetic MNP signals corresponding to this weight vector were generated for the same DF settings and viscosities as in the MPS experiments (see Table 3.1). Ideal transfer functions with unit amplitude and zero phase response over the frequency range were assumed. Zero mean white Gaussian noise was added to the synthetically produced signals in time domain. Two different SNR values of 1 and 10 were considered, mimicking the range of SNR values in MPS experiments. Here, SNR was defined as the ratio of the noise standard deviation to the maximum synthetic

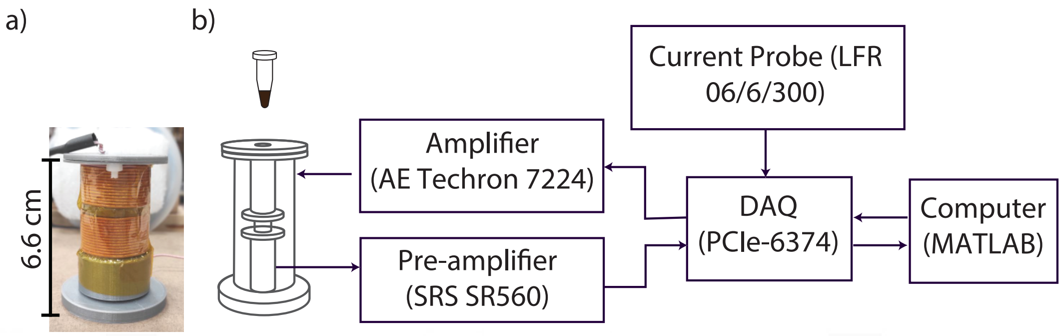

Figure 3.3: Overview of our in-house magnetic particle spectrometer (MPS) setup. (a) A picture of the drive coil. The receive coil is positioned axially inside the drive coil, and its vertical position can be adjusted to minimize mutual inductance between the two coils (b) The workflow of the transmit/receive chain is depicted in the schematic using arrows.

signal amplitude at 0.89 mPa·s for 10 mT and 250 Hz. Finally, the underlying weight vector and transfer functions were estimated from the synthetic signals using the proposed algorithm.

3.2.3 MPS Experiments

The experiments were performed on our in-house MPS setup using samples prepared with two different commercially available MNPs at the same DF settings and viscosity levels as listed in Table 3.1.

MPS Setup

The in-house arbitrary waveform MPS setup, shown in Fig. 3.3, can apply DF waveforms at arbitrary frequencies thanks to the relatively low 13.3 μH inductance of the drive coil, which eliminated the need for impedance matching [60]. The drive coil had 0.66 mT/A sensitivity with 95% homogeneity in a 0.7 cm-long region, measured using a Hall effect gaussmeter (LakeShore 475 DSP Gaussmeter). The receive coil had a two-section gradiometric design, allowing direct feedthrough suppression by manual adjustments. The self-resonance of the receive coil was around 320 kHz.

During data acquisition, the DF waveform designed on MATLAB was sent to the power amplifier (AE Techron 7224) via a data acquisition card (NI USB-6383). The amplified waveform generated the desired DF on the bore of the drive coil. The MNP signal induced on the receive coil was band-pass filtered with filter cutoffs at 100 Hz and 1 MHz and amplified with a low-noise amplifier (SRS SR560) before digitalization via DAQ at a sampling rate of 2 MS/s. A Rogowski current probe (LFR 06/6/300, Power Electronic Measurements Ltd.) was used for adjustment and real-time monitoring of the DF waveform.

Sample Preparation

Experiments were performed using two different MNPs: Vivotrax (Magnetic Insight Inc., USA) and Perimag-plain (Micromod GmbH, Germany) nanoparticles, with 8.5 and 5.5 mg/ml undiluted Fe concentrations, respectively. For each MNP, samples at six different viscosity levels ranging between 0.89-15.33 mPa·s were prepared using glycerol-deionized water (DI) mixtures. All samples used an undiluted nanoparticle volume of 26.2 µl, with glycerol and water added to reach a total volume of 70 µl. The viscosity levels and the corresponding glycerol percentages by volume are given in Table 3.2. The latter were calculated for 25^{o}C using the viscosity formula for glycerol-water mixtures [79], assuming 1.263 g/cm^3 density for glycerol and 0.997 g/cm^3 density for water.

Table 3.2: Glycerol volume percentages at 25^{o}C

Viscosity (mPa·s)	0.89	1.45	2.08	3.32	8.31	15.33
Glycerol vol. (%)	0	15.1	24.8	35.8	53.2	62.5

Experiments

At each DF setting and viscosity, signal measurements were repeated 3 times. Within a single measurement, 8 pulse acquisitions were averaged, with each pulse consisting of 20 DF periods. Before and after each MNP signal measurement, zero-chamber measurements spanning all DF settings were performed. Lastly, a high-order digital low pass filter was applied in time domain with a cut-off frequency set to the frequency of the highest harmonic included. The number of included harmonics, M_k, for each DF setting DF_k was determined with a signal-to-background ratio (SBR) thresholding, where SBR was defined as the ratio of the MNP signal amplitude to the mean zero-chamber signal amplitude at a given harmonic. The SBR threshold was set as 15 in this study, resulting in M_k ranging between 3-33.

MNP Signal Fitting

First, the proposed algorithm was utilized to estimate the weight vectors and transfer functions for Perimag using MPS measurements at all 6 DF settings and 6 viscosity levels. Next, the fitted signal for Perimag was computed using Eq. 3.11. This procedure was then repeated for Vivotrax.

MNP Signal Prediction

The measured Perimag signals from one of the viscosity levels were left out entirely, and the weight vector and transfer functions were estimated with the remaining measurements from other viscosity levels. The signals at the left-out viscosity were then predicted using Eq. 3.13. These steps were repeated by excluding each viscosity level one by one. Then, the same procedure was performed for Vivotrax.

3.2.4 Quantitative Evaluation Metrics

Normalized Root Mean Square Error (NRMSE)

To evaluate the quality of signal predictions, normalized root mean square error (NRMSE) was computed as

$$\mathrm{NRMSE}(\boldsymbol{v}, \hat{\boldsymbol{v}}) = \frac{\|\boldsymbol{v} - \hat{\boldsymbol{v}}\|_2}{\sqrt{n}\,(\max(\boldsymbol{v}) - \min(\boldsymbol{v}))} \tag{3.14}$$

where $\boldsymbol{v}$ and $\hat{\boldsymbol{v}}$ are the measured and fitted/predicted signal vectors in time domain, respectively, and n is the number of samples in one period of the signal. In addition, $\max(\boldsymbol{v})$ and $\min(\boldsymbol{v})$ denote the maximum and minimum values in the vector $\boldsymbol{v}$, respectively.

Relaxation Time Constant (τ)

To assess the similarity of the relaxation dynamics between the measured and fitted/predicted signals, relaxation time constants (τ) were calculated using the TAURUS method [24, 80]. The calculated values were normalized by the DF period and expressed as percentages as

$$\hat{\tau} = \frac{\tau}{T_d} \cdot 100 \tag{3.15}$$

where $T_d = 1/f_d$ is the DF period.

Zero-crossing Time ($\mathbf{t}_{zc}$)

To evaluate the similarity of the signal widths between the measured and fitted/predicted signals, zero-crossing time interval (t_{zc}), defined as the time interval between two zero-crossing points in one-half cycle of a signal, was computed. The resulting values were normalized by the DF period and converted to percentages as

$$\hat{t}_{zc} = \frac{t_{zc}}{T_d} \cdot 100 \tag{3.16}$$

Signal Root Mean Square (v_{rms})

To compare the signal amplitudes, the root mean square amplitude of the signals (v_{rms}) was calculated and normalized as follows:

$$\hat{\mathrm{v}}_{rms} = \frac{\|\boldsymbol{v}\|_2}{\sqrt{n}} \cdot \frac{1}{f_d \cdot B_p \cdot m_{Fe}} \tag{3.17}$$

Note that this computation incorporates expected scalings of the signal with DF frequency and amplitude, as well as with the iron amount in the sample (m_{Fe}(g)).

Normalized Wasserstein Distance

To evaluate the similarity between two weight vectors, normalized Wasserstein distance (NWD) was utilized [81]. This metric, also known as earth mover's distance, provides the cost of turning one probability mass function (PMF) into the other via optimal mass transport. First, the weight vectors were converted to PMFs, i.e., via normalization to ensure unit sum. Then, NWD can be calculated as follows:

$$NWD(\boldsymbol{P_1}, \boldsymbol{P_2}) = \frac{1}{L-1}\|\boldsymbol{F_1} - \boldsymbol{F_2}\|_1 \tag{3.18}$$

Here, $\boldsymbol{P_1}, \boldsymbol{P_2} \in \mathbb{R}^{L\times 1}$ are the compared PMF vectors, $\boldsymbol{F_1}, \boldsymbol{F_2} \in \mathbb{R}^{L\times 1}$ are their corresponding discrete cumulative distribution function (CDF) vectors, and L is the length of these vectors. NWD ranges between 0 and 1, where 0 indicates that the two PMFs are identical and 1 indicates that they are maximally different.

3.2.5 Implementation of the Proposed Algorithm

The maximum number of iterations for the proposed algorithm described in Fig. 3.2(b) was chosen heuristically as 2000 to ensure convergence. For the weight update stage, the built-in function *lsqnonneg* of MATLAB was utilized to solve the NNLS problem given in Eq. 3.9. This function employs an active-set method and utilizes Kuhn-Tucker conditions for least square problems with linear inequality constraints, which is the nonnegativity in our case. The termination tolerance on $\boldsymbol{x}$ set to $10^{-9} \times \left\|\bar{\boldsymbol{A}}\right\|_1 \times \|\bar{\boldsymbol{s}}\|_1$, where $\|\cdot\|_1$ denotes ℓ_1-norm. Note that the tolerance changes at each iteration as $\bar{\boldsymbol{A}}$ changes during the transfer function update stage.

3.3 Results

3.3.1 Validation Results on Synthetic MNP signals

Synthetic MNP signals were generated for a single particle with d_c as 20 nm, d_h as 40 nm, and K as 6 kJ/m^3 (i.e., identical magnetic properties as the particle simulated in Fig. 3.1), at 36 different experimental conditions consisting of 6 different DFs and 6 different viscosities as in MPS measurements (see Table 3.1), assuming unit amplitude and zero phase transfer functions. The synthetic MNP signals were fed to the proposed algorithm. Figure 3.4 shows the estimated weight vectors, transfer functions, and fitted signals for the cases of SNR = 10 and SNR = 1. In Fig. 3.4(a) and 3.4(d), the estimated weight vectors are displayed as marginal PMFs for d_c, K, and d_h. At SNR = 10, the proposed algorithm almost exactly recovers the ground-truth weight vector, whereas there is slight smearing of the PMFs at SNR = 1. The NWDs between the estimated and the ground-truth weight vectors are 0.0007, 0.0009, and 0.0023 for the marginal PMFs of d_c, d_h, and K at SNR = 10. At SNR = 1, the respective NWDs are 0.0088, 0.0159, and 0.0246, demonstrating that the algorithm maintains high fidelity estimations despite the low SNR.

Figures 3.4(b) and 3.4(e) show the transfer functions at 6 different DF settings estimated jointly with the weight vectors at SNR = 10 and SNR = 1, respectively. The amplitudes of the transfer functions remain very close to 1 (0 dB) at both SNR levels, increasing slightly at higher harmonics to a maximum value of 1.01 (0.098 dB) and 1.03 (0.24 dB) at SNR = 10 and SNR = 1, respectively. Similarly, the phases remain very close to zero, reaching a maximum of 0.006 rad and 0.022 rad at higher harmonics at SNR = 10 and SNR = 1, respectively. These slight deviations at higher harmonics are potentially due to reduced signal levels at these harmonics, resulting in a smaller penalty for errors during the optimization process.

Lastly, Figs. 3.4(c) and 3.4(f) show example signals at the settings of 10 mT and 1 kHz, at the viscosity level of 0.89 mPa·s. The spanned signals and fitted signals obtained as described in Eqs. 3.10 and 3.11, respectively, are shown together with the synthetic signals. The fitted signals agree perfectly with the synthetic signal. For this special case of unit amplitude and zero phase transfer functions, the spanned signals also agree with the synthesized signal. The NRMSE values with respect to the ground-truth synthetic signal are 0.01% and 0.1% for the fitted signals at SNR = 10 and SNR = 1,respectively. It should be noted that the ground-truth synthetic signals differ at SNR = 10 vs. SNR = 1 due to different number of harmonics being included as a result of SBR thresholding.

3.3.2 Estimation and Signal Fitting Results for MPS Measurements

Figure 3.5 shows the weight vector, transfer functions, and fitted signals of Perimag and Vivotrax, estimated using measurements from 6 different DF settings and 6 different viscosity levels. The estimated weight vectors are depicted as PMFs for d_c, K, and d_h in Figs. 3.5(a) and 3.5(d), for Perimag and Vivotrax, respectively. Given that both Perimag and Vivotrax are multicore nanoparticles, these distributions can be interpreted as showing the effective magnetic parameters that explain the signals received from these MNPs. The median values for the estimated parameters were d_c = 18 nm, $K = 8\ kJ/m^3$, and d_h = 53 nm for Perimag, and d_c = 21 nm, $K = 9\ kJ/m^3$, and d_h = 44 nm for Vivotrax.

Figures 3.5(b) and 3.5(e) show the harmonic amplitudes and phases of the transfer functions representing the non-model based dynamics for Perimag and

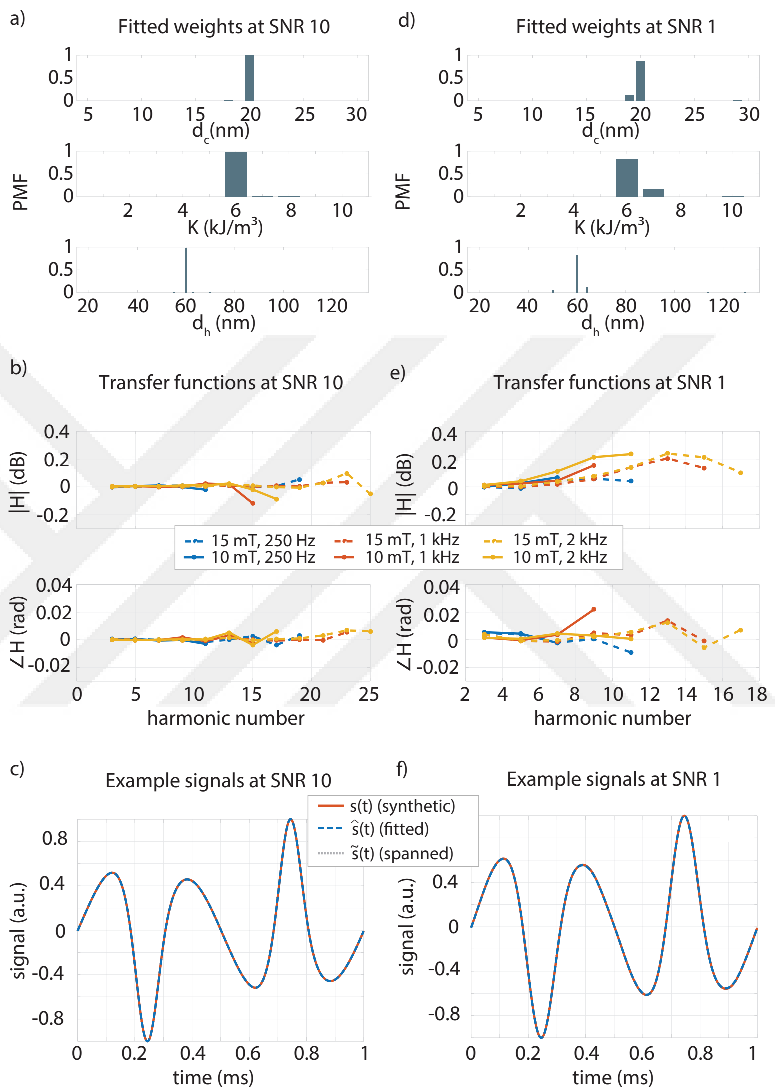

Figure 3.4: Estimated weight vectors, transfer functions, and example signal fitting results for synthetic MNP signals produced for $d_c = 20$ nm, $d_h = 40$ nm, and $K = 6$ kJ/m^3. Estimated weight vectors, shown as PMFs for d_c, d_h, and K, at (a) SNR 10 and (d) SNR 1. Estimated transfer functions amplitudes and phases at (b) SNR 10 and (e) SNR 1. Example spanned, measured, and fitted signals for (c) SNR 10 and (f) SNR 1, at 0.89 mPa·s with 10 mT, 1 kHz as DF. The estimated transfer functions were normalized such that the 3$^{\text{rd}}$ harmonic for 10 mT and 250 Hz would have unit amplitude. The signals spanned by the dictionary, $\tilde{s}(t)$, were scaled to have a maximum amplitude of 1. The measured, $s(t)$, and fitted, $\hat{s}(t)$, signals were normalized together with respect to the maximum amplitude of the measured signal. It should be noted that the scaling between the spanned and fitted/measured signals is arbitrary, so the normalization was performed separately for these two groups.

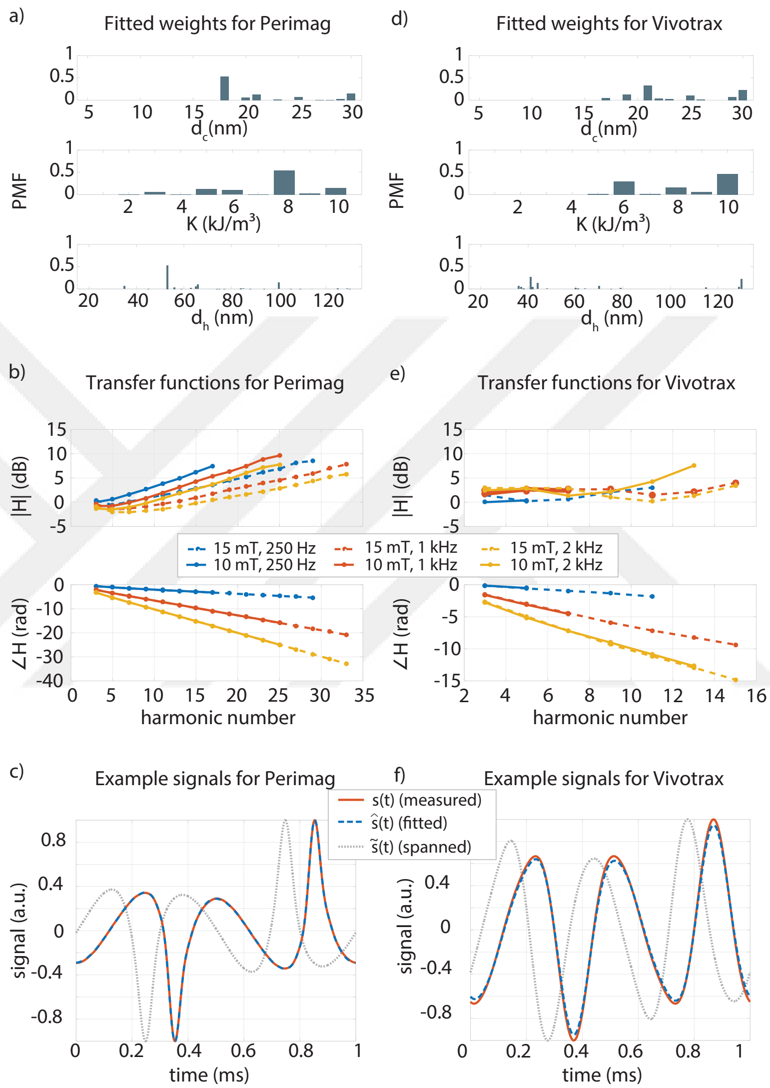

Figure 3.5: Estimated weight vectors, transfer functions, and example signal fitting results for Perimag and Vivotrax. Estimated weight vectors, shown as PMFs for d_c, d_h, and K, for (a) Perimag and (d) Vivotrax. Estimated transfer functions for (b) Perimag and (e) Vivotrax. Example spanned, measured, and fitted signals for (c) Perimag and (f) Vivotrax, at 0.89 mPa·s with 10 mT, 1 kHz as DF. The estimated transfer functions were normalized such that the 3rd harmonic for 10 mT and 250 Hz would have unit amplitude. The signals spanned by the dictionary, $\tilde{s}(t)$, were scaled to have a maximum amplitude of 1. The measured, $s(t)$, and fitted, $\hat{s}(t)$, signals were normalized together with respect to the maximum amplitude of the measured signal. It should be noted that the scaling between the spanned and fitted/measured signals is arbitrary, so the normalization was performed separately for these two groups.

Vivotrax, respectively. Here, due to its reduced signal, the transfer functions for Vivotrax included fewer harmonics when compared to those for Perimag (note the differences in x-axes ranges). While the amplitude of the estimated transfer functions for Vivotrax are remain mostly flat, those for Perimag show a high-pass characteristics. This difference may stem from stronger non-model based dynamics for Perimag, such as dipolar interactions, non-uniaxial magnetic anisotropy, etc. In contrast, the phases of the transfer functions display similar linear trends for both Perimag and Vivotrax, and are nearly independent of the DF amplitude. Given that linear phase is indicative of a time-domain delay, these results imply that the main cause of this delay is the measurement setup itself.

Figures 3.5(c) and 3.5(f) show example signals at 10 mT and 1 kHz DF setting, with 0.89 mPa·s. The spanned and fitted signals, together with the measured MNP signals for Perimag and Vivotrax, respectively are displayed. As expected from the phases of the transfer functions, a similar time delay can be observed between the spanned and measured signals of Perimag and Vivotrax.

In addition, for Perimag, the width of the signal peak is narrower for the fitted signal when compared to the spanned signal, due to the high-pass characteristics of the amplitudes of the transfer functions. Note that, without incorporating the transfer functions into the problem formulation, the estimated weight vector would need to compensate for these effects.

3.3.3 Signal Prediction Results for MPS Measurements

To validate the signal prediction performance of the proposed algorithm, the MPS measurements from each viscosity level was left out one by one, and the signal at that viscosity level was predicted as described in Eqs. 3.12 and 3.13. Example signal prediction results are shown in Fig. 3.6 for Perimag and Vivotrax when the viscosity level of 0.89 mPa·s is left out, for 10 mT and 1 kHz as DF settings. The ground-truth measured signals are also dislayed for reference. The spanned signals once again show a time shift with respect to the measured signal. where as the predicted signals show near perfect temporal alignment, thanks to

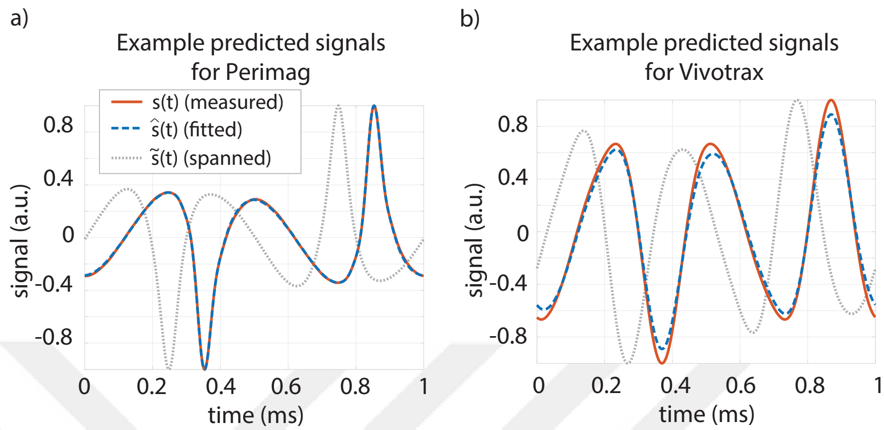

Figure 3.6: (a) Measured, predicted and spanned signals for Perimag at 0.89 mPa·s with 10 mT, 1 kHz as DF. (b) Measured, predicted and spanned signals for Vivotrax at 0.89 mPa·s with 10 mT, 1 kHz as DF.

the estimated transfer function. Overall, the predicted Perimag signal shows a perfect agreement with the measured signal, while the predicted Vivotrax signal underestimates the signal peaks. Correspondingly, the NRMSE(%) values are 0.26% and 2.9% for predicted Perimag and Vivotrax signals, respectively.

3.3.4 Quantitative Assessments for Signal Fitting and Signal Prediction

The results of the quantitative evaluations for fitted and predicted signals with respect to the measured signals are presented in Fig. 3.7 and 3.8 for Perimag and Vivotrax, respectively. The metrics are plotted as functions of the viscosity level, showing the performances at 3 different DF frequencies and 2 different DF amplitudes. The fitted signals at a given viscosity were calculated as described in Eq. 3.11, using the measurements at all DF settings and viscosity measurements. The predicted signals were calculated as described in Eq. 3.13, after excluding all measurements at a given viscosity level.

Results for Perimag

For Perimag, Fig. 3.7(a) shows that the NRMSE(%) values remain below 0.92% and 1.51% for fitted and predicted signals, respectively. The highest errors occur at the extreme experimental conditions, i.e., at the lowest viscosity level at the lowest DF frequency and the highest viscosity level at the highest DF frequency. At the intermediate DF frequency of 1 kHz, the NRMSE remains below 0.43%. Overall, these low NRMSE values indicate a high fidelity match with the measured signal.

To gain a deeper insight regarding performances for signal fitting and signal prediction, Figs. 3.7(b)-(d) compare $\hat{\tau}$, $\hat{t}_{zc}$, and $\hat{\mathrm{v}}_{rms}$ values for measured, fitted, and predicted signals. Overall, these metrics display a strong dependence on viscosity at 250 Hz, $\hat{\tau}$, whereas relatively flatter trends are observed as the DF frequency is increased to 2 kHz. These trends are consistent with previous work in the literature that has shown reduced sensitivity to viscosity at higher DF frequencies [53, 24]. Importantly, these trends are successfully captured by both the fitted and predicted signals. Comparing the metrics from measured, fitted, and predicted signals, one can see an excellent match at all viscosity levels, particularly for $\hat{\tau}$ and $\hat{t}_{zc}$. Comparing the plots Fig. 3.7, we can deduce that the cases of relatively larger NRMSE values Fig. 3.7(a) can be attributed to the mismatch in $\hat{\mathrm{v}}_{rms}$ at those settings.

Results for Vivotrax

Figure 3.8(a) illustrates the NRMSE(%) values of fitted and predicted signals for Vivotrax, which remain below 1.8% and 3.5%, respectively. The highest NRMSE values are observed at extreme viscosities at all DF frequencies. Notably, the NMRSE values for Vivotrax are higher than those of Perimag, which can be attributed to the fewer harmonics being included due to lower SNR of Vivotrax measurement.

Figures 3.8(b)-(d) present $\hat{\tau}$, $\hat{t}_{zc}$, and $\hat{\mathrm{v}}_{rms}$ for the measured, fitted, and predicted signals. In general, $\hat{\tau}$ and $\hat{t}_{zc}$ values are larger than those of Perimag, indicating more substantial relaxation effects for Vivotrax. In addition, $\hat{\mathrm{v}}_{rms}$ is almost 4-fold smaller than that of Perimag, indicating significantly reduced signal per Fe content for Vivotrax. Furthermore, unlike in Perimag, these metrics for Vivotrax maintain a strong dependence on viscosity even at higher DF frequencies. Interestingly, the trends for Vivotrax at 2 kHz are similar to the trends exhibited by Perimag at 250 Hz. This observation implies that Vivotrax experiences similar magnetization dynamics with Perimag but at higher DF frequencies, a results consistent with the literature [53]. Importantly, these trends are successfully captured by both the fitted and predicted signals, albeit with slightly larger errors for the case of Vivotrax than for Perimag.

3.3.5 Quantitative Assessments for Dictionary Weights

The NWD metric was utilized to assess how the estimated dictionary weights are affected by the process of excluding all measurements from a given viscosity level. Since ground-truth weights are not available, the weight vectors obtained by including all available measurements were utilized as the references (i.e., as shown in Figs. 3.5(a) and 3.5(d) for Perimag and Vivotrax, respectively).

NWDs for marginal PMF of d_c, K, and d_h, as well their joint PMF are shown in Fig. 3.9, as functions of the excluded viscosity level. Overall, NWD remains below 0.10 and 0.07 for Perimag and Vivotrax, respectively. Specifically, for the marginal PMF of d_c, NWD remains below 0.03 and 0.04 for Perimag and Vivotrax, respectively. The viscosity levels that, when excluded, lead to a relatively larger deviation in the estimated weight vector differ for Perimag and Vivotrax. For Vivotrax, including the highest and lowest viscosity levels are more important to obtain weights that are closer to the reference. In contrast, including the low-to-mid viscosity levels are more important for Perimag. To illustrate, for the joint PMFs, the highest NWD of 0.08 occurs at 2.08 mPa·s for Perimag and the highest NWD of 0.05 occurs at 15.33 mPa·s for Vivotrax. Nonetheless, the NWD values

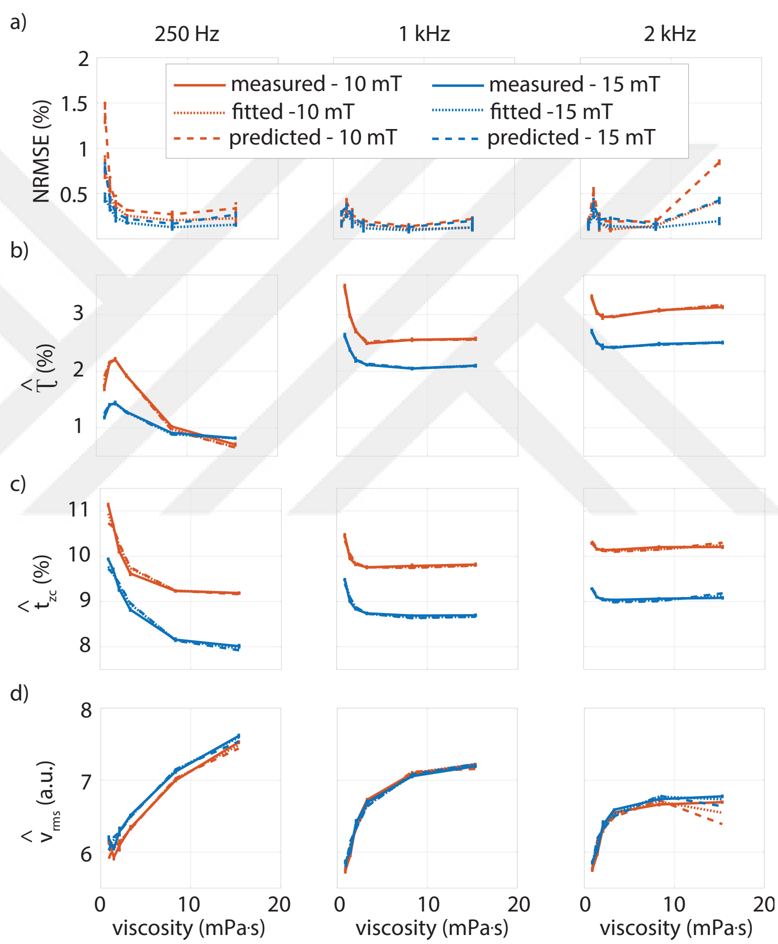

Figure 3.7: Quantitative assessment of signal prediction and fitting for Perimag at 3 different DF frequencies and 2 different DF amplitudes plotted as a function of sample viscosities. The predicted signal at a given viscosity corresponds to the signal predicted by leaving the corresponding viscosity out in Eq. 3.2. The fitted signals were obtained by including all available measured signals in Eq. 3.2 (a) $\hat{\tau}$, (b) $\hat{t}_{zc}$ and (c) $\hat{v}_{rms}$ for measured, predicted and fitted signals. (d) NRMSE of predicted and fitted signals, taking measured signal as the reference.

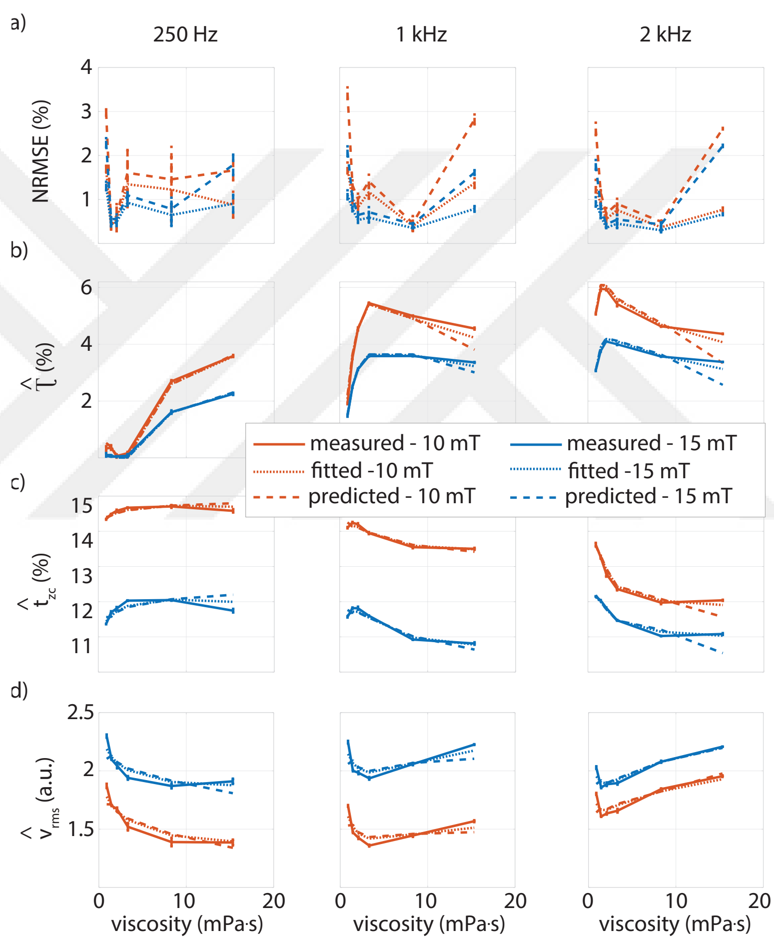

Figure 3.8: Quantitative assessment of signal prediction and fitting for Vivotrax at 3 different DF frequencies and 2 different DF amplitudes plotted as a function of sample viscosities. The predicted signal at a given viscosity corresponds to the signal predicted by leaving the corresponding viscosity out in Eq. 3.2. The fitted signals were obtained by including all available measured signals in Eq. 3.2 (a) $\hat{\tau}$, (b) $\hat{t}_{zc}$ and (c) $\hat{v}_{rms}$ for measured, predicted and fitted signals. (d) NRMSE of predicted and fitted signals, taking measured signal as the reference.

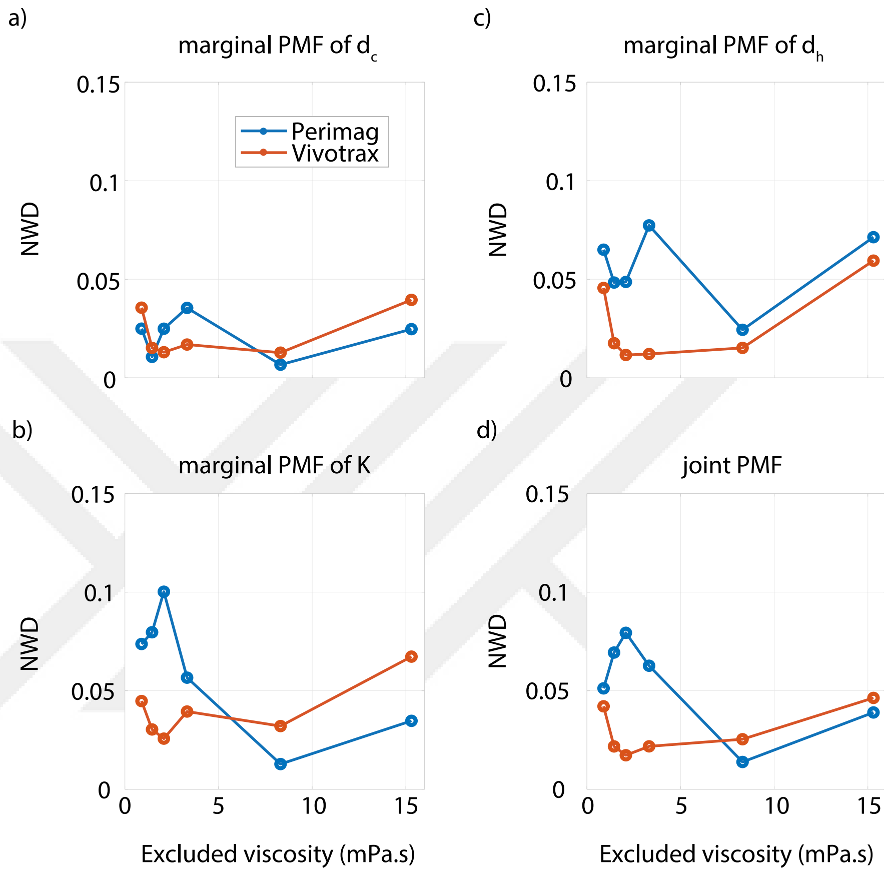

Figure 3.9: NWDs for Perimag and Vivotrax, calculated for (a) marginal d_c, (b) marginal K, (c) marginal d_h,(d) joint PMFs.

remain low for all cases, indicating a robustness in dictionary weight estimation, particularly for the estimation of the weights for d_c.

3.4 Discussion

In this work, we have proposed a novel calibration-free dictionary-based algorithm for MNP signal prediction. In addition to the model-based dynamics, the proposed approach incorporates the non-model based dynamics by modeling them as an LTI system, and simultaneously estimates the dictionary weight vector and transfer functions. The predicted signals at all viscosity levels demonstrate an excellent match with the measured signal, successfully capturing the trends as a function of viscosity.

3.4.1 Magnetization Model

In this work, a coupled Brown-Néel rotation model was utilized to construct the dictionaries. As shown in the magnetization simulations in Fig. 3.1, the coupled model captures unique magnetization characteristics compared to simpler models. The MPS experiments further reaffirm the necessity of utilizing the coupled model, as they demonstrate that the MNPs experience both Brown and Néel rotations for the range of DF settings utilized in this work. As illustrated in Fig. 3.7 for Perimag, lower DF frequencies display a strong viscosity sensitivity that implies Brown rotation taking place. In contrast, the viscosity sensitivity diminishes as DF frequency increases to 2 kHz, suggesting that the Brown rotation becomes less effective and is superseded by Néel rotation.

Note that the pure Néel model and the Langevin model do not incorporate the viscosity effect on the magnetization, and hence are not suitable for the purposes of this study. To test whether the pure Brown model would suffice in capturing the trends, we formed dictionaries by using this model, simulating the magnetization responses for the same set of magnetic parameters. Since the pure Brown model does not incorporate the anisotropy effect, K was not included as a parameter [40, 28]. The signal prediction performance using the pure Brown model was poor, yielding fitted and predicted signals that both diverged from the measured signals (results not shown).

3.4.2 Non-Model-Based Dynamics

While it provides a powerful framework for understanding the MNP responses, the coupled Brown-Néel rotation model is not without its own limitations. It assumes uniaxially symmetric particles with uniaxial magnetic anisotropy due to their shape anisotropy [47]. Although magnetite and maghemite, the most commonly used iron oxides in MPI, exhibit cubic crystal symmetry, the resulting anisotropy is ignored due to the relatively low energy barrier in the crystal [38]. Furthermore, the employed model assumes single-core particles, whereas Perimag and Vivotrax are both multicore MNPs. In this work, these multicore MNPs were treated as single-core particles with an effective d_c, as commonly done in the literature [74, 82, 83, 84]. Nevertheless, the interactions among the multi-core MNPs are not accounted for by the employed model.

The proposed algorithm hypothesizes that the effects of the non-model-based dynamics can be formulated as an LTI system that accounts for (1) the magnetization dynamics that are not accounted for by the employed magnetization model and (2) the transfer function of the measurement setup. The LTI assumption holds for the measurement setup, since it is composed of linear circuit components.

The LTI assumption for the non-model-based magnetization dynamics, such as magnetodipolar interactions and dynamics resulting from nonuniaxial magnetic anisotropy, deserves a closer look. For practical purposes such as enabling signal prediction at different viscosities, the formulation in Eq. 3.2 assumes that these dynamics are dependent on the DF settings, but not on the viscosity level. The quantitative and qualitative evaluations conducted on fitted and predicted signals in Figs. 3.6-3.8 confirm the effectiveness of this approach for the employed range of DF settings and viscosities. Nonetheless, the relatively reduced fitting and prediction performances at the highest/lowest viscosities in Figs. 3.7-3.8 may imply that this assumption may not be fully valid for a wider range of viscosities.

The validation results on synthetic signals, shown in Fig. 3.4, illustrate that the proposed algorithm can simultaneously estimate the underlying weight vector and the transfer functions. When synthetic signals were generated for the same magnetic parameters but with transfer functions having polynomial amplitudes and linear phases, the proposed algorithm was still successful in estimating the weight vector and the transfer functions (results not shown).

For the experimental results, the ground-truth weight vectors and transfer functions are not known. The estimated transfer functions for Perimag show high-pass characteristics, which are not present in those for Vivotrax (see Fig. 3.5). The high-pass characteristics imply that non-model-based magnetization dynamics contribute to improving the MPI resolution of Perimag. This observation is consistent with the literature reporting improved MPI resolution for this MNP due to increased dipolar interactions [85, 86]. Note that if the employed magnetization model could fully capture the magnetization dynamics, the estimated transfer functions would solely represent those of the measurement setup, and would therefore be identical for different MNPs. While the system transfer function could be determined via additional calibration measurements [87], the proposed algorithm has the advantage of characterizing the measurement setup in a calibration-free manner.

3.4.3 Magnetic Parameters

The proposed algorithm relies on a dictionary of simulated MNP signals. The range of parameters given in Table 3.1 were selected to safely cover the typical values reported in the literature [74, 88]. It should be noted that particles with different magnetic parameters may display similar magnetization responses, which in turn may make the inverse problem ill-conditioned. This problem can further be exacerbated if the measured signal has low SNR. In such a case, fewer harmonics survive SBR thresholding, causing the system of equations to be highly underdetermined. One potential approach to solve this problem could be to optimize the range and sampling of the magnetic parameters based on the SNR level, with the goal of improving the conditioning of the dictionary matrix. A detailed analysis on how the selection of the magnetic parameters affect the accuracy of signal prediction, as well as how the SNR level interplays with this selection, remains an important future work.

It can also be challenging to estimate the weights for particles with very small core diameters, which contribute to the iron content but do not contribute significantly to the measured signal. The proposed algorithm may assign low weights to these particles, making it difficult to determine the total iron content in the sample. However, this problem would not pose a restriction for signal prediction purposes, which is the main goal of this work.

Chapter 4

MNP Signal Prediction at Untested Drive Field Settings

This chapter is based on the following publication:

A. Alpman, M. Utkur, E.U. Saritas. "A Dictionary-Based Algorithm for MNP Signal Prediction At Unmeasured Drive Field Frequencies", Proc of the 12th International Workshop on Magnetic Particle Imaging, Aachen, Germany, p. 2303004, March 2023. DOI: 10.18416/IJMPI.2023.2303004

4.1 Background

Previous work has shown that applications of MPI, such as relaxation-based viscosity mapping and temperature mapping, may have optimal drive field (DF) frequencies that are different than the commonly used 25 kHz [25, 24]. However, determining the optimal DF settings requires extensive experimental measurements. To better understand the trends in the MNP response, accurate modeling of the underlying physics is crucial. Previous work employed model-based simulation approaches to explain the magnetic response and estimate the parameters of MNPs [89, 45, 48].

This chapter proposes a dictionary-based method that also accounts for measurement system response to estimate the parameters that give rise to the measured MNP signal. In addition, an empirical method is proposed to predict the system response at DF frequencies where no measurement data is available, enabling MNP signal prediction unmeasured DF frequencies.

4.2 Methods

4.2.1 Dictionary Preparation

The magnetization responses of MNPs with varying magnetic parameters under sinusoidal DFs were simulated by solving ordinary differential equation, given in [47], derived from the Fokker-Planck equations of a coupled Brown-Néel rotation model, as described in Section 2.3.4. The simulated MNPs had uniaxial magnetic anisotropy constant (K) ranging from 1 to 10 kJ/m^3, core diameter (d_c) ranging from 5 to 30 nm, and hydrodynamic diameter (d_h) ranging from 20 to 130 nm. In total, the responses for 4680 different MNPs were simulated. The response of each MNP was simulated at 6 different DFs with 10 mT and 15 mT amplitude and 250 Hz, 1 kHz, and 2 kHz frequency. These relatively low frequencies were chosen, as they were previously shown to have high viscosity sensitivity [53, 24]. In addition, the simulations were repeated at 6 different viscosity levels (η) ranging from 0.89 to 15.33 mPa·s. The Gilbert damping constant, saturation magnetization, and temperature were assumed to be 0.1, 360 kA/m, and 25°C, respectively. At the considered frequencies, the coupled Brown-Neel rotation model provided considerably different MNP signals than the simpler Brown-only and Langevin models, underscoring the importance of accurate modeling.

4.2.2 Problem Formulation

Assuming that the measurement setup can be modeled as a linear time-invariant (LTI) system, we formulated the problem in the frequency domain to solve simultaneously for the transfer function (TF) of the measurement setup and the dictionary weights. Note that the TFs vary with the DF settings, since both the transmit and receive chain characteristics change with the applied DF amplitude and frequency. While the estimated weights enable us to estimate the magnetic parameters of the tested MNP, the estimated TF allows us to characterize the system in a calibration-free manner. We formulate this problem as follows:

$$\min_{x \in \mathbb{R}^{n\times 1}, H \in \mathbb{R}^{m\times m}} \quad \|HAx - b\|_2^2 \quad \text{s.t.} \quad x \geq 0 \tag{4.1}$$

where $A \in \mathbb{R}^{m\times n}$ is the dictionary matrix constructed with the simulated MNP signals, $b \in \mathbb{R}^{m\times 1}$ is the measurement vector with concatenated experimental data from different viscosity levels, $H \in \mathbb{R}^{m\times m}$ is the diagonal matrix with the TF values as diagonal entries, n is the number of MNPs in the dictionary, m is the total number of harmonics used for parameter estimation, and $x \in \mathbb{R}^{n\times 1}$ is the vector of dictionary weights. To integrate different DFs into the problem, we concatenated the corresponding matrices from the different DFs vertically. Then, we simultaneously solved for H and a common optimal x using alternating minimization methods, i.e., keeping one variable fixed while the other variable is optimized. It should be noted that there are infinitely many (x, H) pairs that satisfy Eq. 1 but have different scalings, i.e., $(kx, H/k)$ for some arbitrary constant k. However, such a scaling does not affect the MNP signal prediction results since x and H are eventually multiplied for signal prediction purposes.

4.2.3 Transfer Function and Signal Prediction

Unless we have measured data at a specific DF, the TF for that DF can not be obtained via Eq 4.1. For this purpose, we propose an empirical method that predicts the TF at an unmeasured DF frequency and amplitude using the previously estimated TFs at measured DF frequencies with the same amplitude. Accordingly, at each harmonic number, a linear fit is performed to the estimated TF amplitude in logarithmic scale versus the DF frequency in logarithmic scale at the measured DFs. The TF amplitude at the unmeasured DF is then predicted using this linear fit.

For the MNP signal prediction at the unmeasured DF, first a response is simulated considering the dictionary weights. The predicted TF amplitude is then applied to this response to predict the MNP signal.

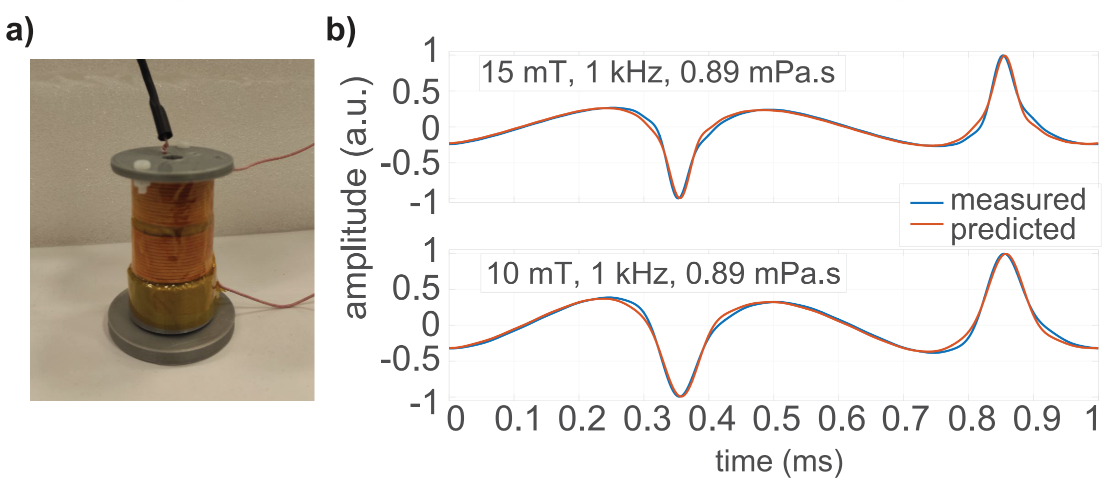

Figure 4.1: *(a) In-house arbitrary waveform MPS setup. (b) Example measured and predicted signals (normalized together) for the sample at 0.89 mPa·s viscosity level, at two different field amplitudes at 1 kHz DF frequency.*

4.2.4 Quantitative Assessments

Note that we only predict the amplitude of the TF, while directly assigning zero phase to each harmonic to simplify the problem. Since we observed a linear phase response for the TF solutions, ignoring the phase of the TF causes the predicted signal to only be shifted in time. Therefore, a time shift is applied to the predicted signal to quantitatively compare its accuracy with respect to the reference signal (i.e., the actual measured signal at that DF setting). As a quantitative evaluation metric, normalized root mean square error (NRMSE) between the measured and predicted signals was utilized.

As a second metric, we compared the normalized root mean square (RMS) amplitudes of the signals as follows:

$$\hat{s}_{rms} = \frac{1}{f_d(Hz) \cdot B_d(T) \cdot Fe(g)} \times \sqrt{\frac{1}{N}\sum_{n=1}^{N} s_n^2} \tag{4.2}$$

Here, the RMS signal is normalized by DF frequency f_d, DF amplitude B_d, and iron content Fe. Lastly, we compared the time interval between two zero crossing time points in a one-half cycle, t_{zc}. To enable comparison relative to DF period T_d, we defined percentage zero-crossing time interval as:

$$\hat{t}_{zc} = \frac{t_{zc}}{T_d} \times 100 \tag{4.3}$$

4.3 Experiments

The experiments were performed on an in-house arbitrary waveform magnetic particle spectrometer (MPS) setup, shown in Fig. 4.1a. The power amplifier (AE Techron 7224) amplifies the DF waveform from the data acquisition card (NI USB-6383) and sends it to the DF coil. The received signal is amplified by a low-noise amplifier (SRS SR560) and sent to a PC to be processed in MATLAB. The experiments were conducted at 10 mT and 15 mT DF amplitudes, at 250

Hz, 1 kHz, and 2 kHz DF frequencies. MNP samples at 6 different viscosity levels were prepared using glycerol and deionized water [79], with each sample containing 26.2 µl of Perimag nanoparticles (Micromod GmbH, Germany) with a total volume of 70 µl.

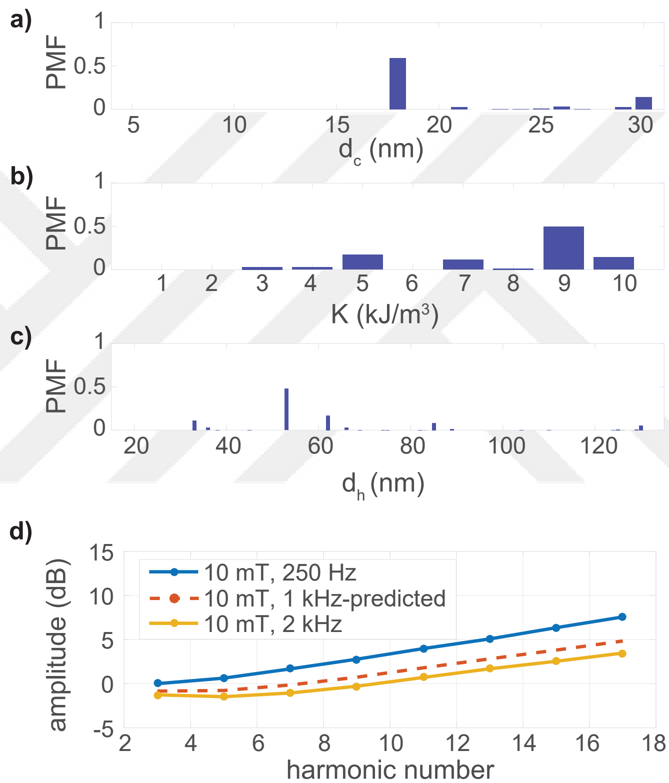

Figure 4.2: *MNP parameter and TF estimation results when 1 kHz DF measurements are left out. The probability mass functions for (a) d_c, (b) K, and (c) d_h are displayed. (d) Estimated TF amplitude at 250 Hz and 2 kHz, at 10 mT amplitude. TF amplitudes were normalized with respect to the TF value at the third harmonic of 250 Hz. The dashed line shows the predicted TF amplitude at 1 kHz.*

4.4 Results and Discussion

Figure 4.1b shows the predicted and measured signals at 1 kHz for 0.89 mPa·s viscosity level. The signal predictions work accurately throughout the period, with the exception of slight mismatches in the signal tails. Figure 4.2 shows the estimated MNP parameter distribution and the TF amplitudes for the case where 1 kHz DF measurements are left out, together with the predicted TF amplitude at 1 kHz. We observed that the estimated parameter distribution varies only slightly depending on the left out DF frequency. For example, the mean core diameters were 19.9 nm, 21.1 nm, and 20.9 nm for the left out frequencies 250 Hz, 1 kHz, and 2 kHz, respectively.

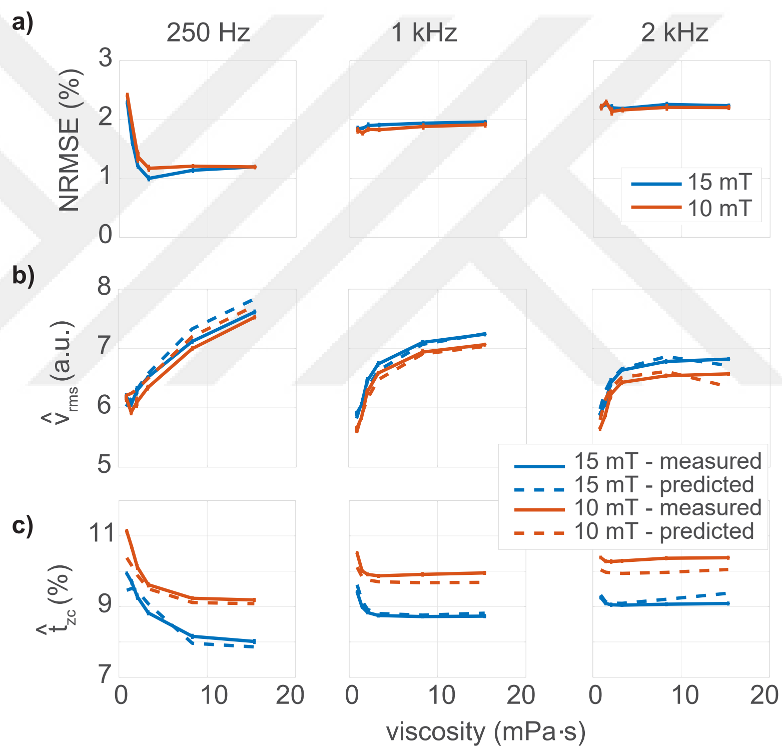

Figure 4.3: *Signal prediction accuracy at 3 DF frequencies and 2 DF amplitudes, plotted as a function of sample viscosity. (a) NRMSE of prediction, and (b)* $\hat{s}_{rms}$ *and (c)* $\hat{t}_{zc}$ *for the predicted and measured signals. In each case, measurements at the relevant DF frequency were entirely left out during prediction.*

Figure 4.3 shows the quantitative assessment results for the prediction. For each case, measurements at the relevant DF frequency were entirely left out during parameter estimation and signal prediction. The predicted response was then compared with the actual measured response at that DF setting. Overall, the signal prediction works successfully at a wide range of DF settings. Accordingly, NMRSE for the signal prediction remains below 3% at all viscosity levels and DF settings. Evaluations on $\hat{s}_{rms}$ and $\hat{t}_{zc}$ also demonstrate a close match between the measured and predicted signals, but also provide better insight regarding the differences between the measured and predicted signals. To illustrate, while NMRSE remains near constant at all viscosity levels at 2 kHz, both $\hat{s}_{rms}$ and $\hat{t}_{zc}$ demonstrate a slight deviation between the measured and predicted signals at the highest viscosity.

In this work, we modeled MNPs as single core spherical particles with uniaxial magnetic anisotropy. Therefore, the estimated distributions in Fig. 4.2a-c are for "effective parameters" that may not have a full physical correspondence, especially in the case of multicore MNPs. Nonetheless, the quantitative assessments in Fig. 4.2 demonstrate that these effective parameters successfully capture the trends in MNP signal at different DF settings. Overall, the results indicate that the proposed method works successfully in predicting TFs and MNP signals. Further verification of the proposed method at a wider range of DF settings remains as future work.

Chapter 5

Conclusion and Future Work

This thesis proposed a calibration-free iterative dictionary-based algorithm that simultaneously estimates the dictionary weights and non-model based dynamics, allowing MNP signal predictions at untested settings. The quantitative and qualitative assessments on synthesized and measured signals demonstrate the accuracy of the proposed approach in predicting the trends in MNP signal as a function of viscosity and at different DF settings. This approach offers numerous potential applications, such as determining the optimal DF settings or optimal MNPs for viscosity mapping and temperature mapping using MPI.

Simulating the dictionary matrix that is at the heart of the proposed method requires extensive computation time. For example, solving the ODE underlying the coupled Brown-Néel model can take anywhere from minutes to a few days for a single particle, depending on its magnetic parameters. Particularly, it takes longer to simulate the magnetic responses for particles with large d_c and large K. The computational burden can restrict the practicality of the proposed algorithm in predicting signal trends under a wide range of settings. In this work, we have utilized parallelization on a CPU using 4-8 cores to simultaneously simulate particles with different parameters. Further reduction in computation time could be achieved using GPUs and/or faster ODE solvers [90]. Alternatively, deep learning based approaches for simulating the magnetization response can be utilized, offering upto 200 fold reduction in computation time [91].

The proposed algorithm explains and predicts the impact of viscosity on the MNP signals measured with MPS. One application of the proposed algorithm is to accurately determine the signal trends in a wide range of viscosities and DF settings, from measurements performed at only a few different viscosities and DF settings. Building upon this approach, the trends in the MNP signal as a function of temperature can also be predicted using the same algorithm, using measurements performed at only a few different temperatures and DF settings.

The same framework can also be extended to MPI signal prediction. This extension would require simulations that incorporate not only the DF but also the selection field of the MPI system. In the end, MPI signal prediction can help guide applications such as viscosity mapping and temperature mapping. For example, imaging experiments could be performed at a few different DF settings with a restricted number of samples at different viscosities. Signal prediction can then determine the trends at a wider range of viscosities and DF settings, revealing the optimal DF settings for mapping viscosity with MPI.

Bibliography

[1] B. Gleich and J. Weizenecker, "Tomographic imaging using the nonlinear response of magnetic particles," *Nature*, vol. 435, no. 7046, p. 1214–1217, 2005.

[2] B. Gleich, J. Weizenecker, and J. Borgert, "Experimental results on fast 2d-encoded magnetic particle imaging," *Physics in Medicine and Biology*, vol. 53, no. 6, p. N81–N84, 2008.

[3] J. Weizenecker, B. Gleich, J. Rahmer, H. Dahnke, and J. Borgert, "Three-dimensional real-time in vivo magnetic particle imaging," *Physics in Medicine and Biology*, vol. 54, no. 5, p. L1–L10, 2009.

[4] P. W. Goodwill and S. M. Conolly, "The x-space formulation of the magnetic particle imaging process: 1-D signal, resolution, bandwidth, SNR, SAR, and magnetostimulation," *IEEE Transactions on Medical Imaging*, vol. 29, no. 11, pp. 1851–1859, 2010.

[5] E. U. Saritas, P. W. Goodwill, L. R. Croft, J. J. Konkle, K. Lu, B. Zheng, and S. M. Conolly, "Magnetic particle imaging (mpi) for nmr and mri researchers," *Journal of Magnetic Resonance (San Diego, Calif.: 1997)*, vol. 229, p. 116–126, 2013.

[6] B. Zheng, T. Vazin, P. W. Goodwill, A. Conway, A. Verma, E. U. Saritas, D. Schaffer, and S. M. Conolly, "Magnetic particle imaging tracks the long-term fate of in vivo neural cell implants with high image contrast," *Scientific Reports*, vol. 5, p. 14055, 2015.

[7] K. Them, J. Salamon, P. Szwargulski, S. Sequeira, M. G. Kaul, C. Lange, H. Ittrich, and T. Knopp, "Increasing the sensitivity for stem cell monitoring in system-function based magnetic particle imaging," *Physics in Medicine and Biology*, vol. 61, no. 9, p. 3279–3290, 2016.

[8] Q. Wang, X. Ma, H. Liao, Z. Liang, F. Li, J. Tian, and D. Ling, "Artificially engineered cubic iron oxide nanoparticle as a high-performance magnetic particle imaging tracer for stem cell tracking," *ACS Nano*, vol. 14, no. 2, p. 2053–2062, 2020.

[9] O. C. Sehl, J. J. Gevaert, K. P. Melo, N. N. Knier, and P. J. Foster, "A perspective on cell tracking with magnetic particle imaging," *Tomography*, vol. 6, no. 4, p. 315–324, 2020.

[10] S. Herz, P. Vogel, P. Dietrich, T. Kampf, M. A. Rückert, R. Kickuth, V. C. Behr, and T. A. Bley, "Magnetic particle imaging guided real-time percutaneous transluminal angioplasty in a phantom model," *CardioVascular and Interventional Radiology*, vol. 41, no. 7, p. 1100–1105, 2018.

[11] I. Molwitz, H. Ittrich, T. Knopp, T. Mummert, J. Salamon, C. Jung, G. Adam, and M. G. Kaul, "First magnetic particle imaging angiography in human-sized organs by employing a multimodal ex vivo pig kidney perfusion system," *Physiological Measurement*, vol. 40, no. 10, p. 105002, 2019.

[12] A. Mohtashamdolatshahi, H. Kratz, O. Kosch, R. Hauptmann, N. Stolzenburg, F. Wiekhorst, I. Sack, B. Hamm, M. Taupitz, and J. Schnorr, "In vivo magnetic particle imaging: angiography of inferior vena cava and aorta in rats using newly developed multicore particles," *Scientific Reports*, vol. 10, no. 1, 2020.

[13] E. Y. Yu, M. Bishop, B. Zheng, R. M. Ferguson, A. P. Khandhar, S. J. Kemp, K. M. Krishnan, P. W. Goodwill, and S. M. Conolly, "Magnetic particle imaging: A novel in vivo imaging platform for cancer detection," *Nano letters*, vol. 17, no. 3, p. 1648–1654, 2017.

[14] X. Zhu, J. Li, P. Peng, N. H. Nassab, and B. R. Smith, "Quantitative drug release monitoring in tumors of living subjects by magnetic particle imaging nanocomposite," *Nano letters*, vol. 19, no. 10, p. 6725–6733, 2019.

[15] Z. W. Tay, P. Chandrasekharan, B. D. Fellows, I. R. Arrizabalaga, E. Yu, M. Olivo, and S. M. Conolly, "Magnetic particle imaging: An emerging modality with prospects in diagnosis, targeting and therapy of cancer," *Cancers*, vol. 13, no. 21, p. 5285, 2021.

[16] P. Chandrasekharan, Z. W. Tay, D. Hensley, X. Y. Zhou, B. K. Fung, C. Colson, Y. Lu, B. D. Fellows, Q. Huynh, C. Saayujya, E. Yu, R. Orendorff, B. Zheng, P. Goodwill, C. Rinaldi, , and S. Conolly, "Using magnetic particle imaging systems to localize and guide magnetic hyperthermia treatment: tracers, hardware, and future medical applications," *Theranostics*, vol. 10, no. 7, p. 2965–2981, 2020.

[17] G. Song, M. Kenney, Y.-S. Chen, X. Zheng, Z. C. Yong Deng, S. X. Wang, S. S. Gambhir, H. Dai, and J. Rao, "Carbon-coated feco nanoparticles as sensitive magnetic-particle-imaging tracers with photothermal and magnetothermal properties," *Nature Biomedical Engineering*, vol. 4, no. 3, p. 325–334, 2020.

[18] Y. Lu, A. Rivera-Rodriguez, Z. W. Tay, D. Hensley, K. L. B. Fung, C. Colson, C. Saayujya, Q. Huynh, L. Kabuli, B. Fellows, P. Chandrasekharan, C. Rinaldi, and S. Conolly, "Combining magnetic particle imaging and magnetic fluid hyperthermia for localized and image-guided treatment," *International Journal of Hyperthermia*, vol. 37, no. 3, p. 141–154, 2020.

[19] A. C. Bakenecker, M. Ahlborg, C. Debbeler, C. Kaethner, T. M. Buzug, and K. Lüdtke-Buzug, "Magnetic particle imaging in vascular medicine," *Innovative Surgical Sciences*, vol. 3, no. 3, p. 179–192, 2018.

[20] J. Salamon, J. Dieckhoff, M. G. Kaul, C. Jung, G. Adam, M. Möddel, T. Knopp, S. Draack, F. Ludwig, and H. Ittrich, "Visualization of spatial and temporal temperature distributions with magnetic particle imaging for liver tumor ablation therapy," *Scientific Reports*, vol. 10, no. 1, p. 7480, 2020.

[21] F. Wegner, K. Lüdtke-Buzug, S. Cremers, T. Friedrich, M. M. Sieren, J. Haegele, M. A. Koch, E. U. Saritas, P. Borm, T. M. Buzug, J. Barkhausen, and M. Ahlborg, "Bimodal interventional instrument markers for magnetic particle imaging and magnetic resonance imaging—a proof-of-concept study," *Nanomaterials*, vol. 12, no. 10, p. 1758, 2022.

[22] D. B. Mangarova, J. Brangsch, A. Mohtashamdolatshahi, O. Kosch, H. Paysen, F. Wiekhorst, R. Klopfleisch, R. Buchholz, U. Karst, M. Taupitz, J. Schnorr, B. Hamm, and M. R. Makowski, "Ex vivo magnetic particle imaging of vascular inflammation in abdominal aortic aneurysm in a murine model," *Scientific Reports*, vol. 10, no. 1, 2020.

[23] P. Chandrasekharan, K. L. B. Fung, X. Y. Zhou, W. Cui, C. Colson, D. Mai, K. Jeffris, Q. Huynh, C. Saayujya, L. Kabuli, B. Fellows, Y. Lu, E. Yu, Z. W. Tay, B. Zheng, L. Fong, and S. M. Conolly, "Non-radioactive and sensitive tracking of neutrophils towards inflammation using antibody functionalized magnetic particle imaging tracers," *Scientific Nanotheranostics*, vol. 5, no. 2, p. 240–255, 2021.

[24] M. Utkur and E. U. Saritas, "Simultaneous temperature and viscosity estimation capability via magnetic nanoparticle relaxation," *Medical Physics*, vol. 49, no. 4, pp. 2590–2601, 2022.

[25] M. Utkur, Y. Muslu, and E. U. Saritas, "Relaxation-based color magnetic particle imaging for viscosity mapping," *Applied Physics Letters*, vol. 115, p. 152403, 10 2019.

[26] W. F. Brown, "Thermal fluctuations of a single-domain particle," *Phys. Rev.*, vol. 130, pp. 1677–1686, Jun 1963.

[27] W. T. Coffey, P. J. Cregg, and Y. P. Kalmykov, "On the theory of debye and néel relaxation of single domain ferromagnetic particles," *Advances in Chemical Physics*, vol. 83, pp. 263–464, 2007.

[28] C. Shasha and K. M. Krishnan, "Nonequilibrium dynamics of magnetic nanoparticles with applications in biomedicine," *Advanced Materials*, vol. 33, no. 23, p. 1904131, 2020.

[29] D. V. Berkov, N. L. Gorn, R. Schmitz, and D. Stock, "Langevin dynamic simulations of fast remagnetization processes in ferrofluids with internal magnetic degrees of freedom," *Journal of Physics: Condensed Matter*, vol. 18, no. 38, p. S2595–S2621, 2006.

[30] S. Ota, T. Yamada, and Y. Takemura, "Dipole-dipole interaction and its concentration dependence of magnetic fluid evaluated by alternating current hysteresis measurement," *Journal of Applied Physics*, vol. 117, no. 17, p. 17D713, 2015.

[31] K. Wu, D. Su, R. Saha, J. Liu, and J. Wang, "Investigating the effect of magnetic dipole–dipole interaction on magnetic particle spectroscopy: implications for magnetic nanoparticle-based bioassays and magnetic particle imaging," *Journal of Physics D: Applied Physics*, vol. 52, no. 33, p. 335002, 2019.

[32] C. Shasha, E. Teeman, and K. M. Krishnan, "Nanoparticle core size optimization for magnetic particle imaging," *Biomedical Physics & Engineering Express*, vol. 5, no. 5, p. 055010, 2019.

[33] E. Teeman, C. Shasha, J. E. Evans, and K. M. Krishnan, "Intracellular dynamics of superparamagnetic iron oxide nanoparticles for magnetic particle imaging," *Nanoscale*, vol. 11, no. 16, p. 7771–7780, 2019.

[34] L. Moor, S. Scheibler, L. Gerken, K. Scheffler, F. Thieben, T. Knopp, I. K. Herrmann, and F. H. L. Starsich, "Particle interactions and their effect on magnetic particle spectroscopy and imaging," *Nanoscale*, vol. 14, no. 19, p. 7163–7173, 2022.

[35] S. Biederer, T. Knopp, T. F. Sattel, K. Lüdtke-Buzug, B. Gleich, J. Weizenecker, J. Borgert, and T. M. Buzug, "Magnetization response spectroscopy of superparamagnetic nanoparticles for magnetic particle imaging," *Journal of Physics D: Applied Physics*, vol. 42, no. 20, p. 205007, 2009.

[36] J. Weizenecker, B. Gleich, J. Rahmer, and J. Borgert, "Particle dynamics of mono-domain particles in magnetic particle imaging," *Magnetic Nanoparticles*, pp. 3–15, 2010.

[37] D. B. Reeves and J. B. Weaver, "Simulations of magnetic nanoparticle Brownian motion," *Journal of Applied Physics*, vol. 112, 12 2012.

[38] J. Weizenecker, B. Gleich, J. Rahmer, and J. Borgert, "Micro-magnetic simulation study on the magnetic particle imaging performance of anisotropic mono-domain particles," *Physics in Medicine and Biology*, vol. 57, no. 55, pp. 7317–7327, 2012.

[39] M. A. Martens, R. J. Deissler, Y. Wu, L. Bauer, Z. Yao, R. Brown, and M. Griswold, "Modeling the brownian relaxation of nanoparticle ferrofluids: Comparison with experiment," *Medical Physics*, vol. 40, no. 2, p. 022303, 2013.

[40] R. J. Deissler, Y. Wu, and M. Martens, "Dependence of brownian and néel relaxation times on magnetic field strength," *Medical Physics*, vol. 41, no. 1, p. 012301, 2013.

[41] M. Graeser, K. Bente, and T. M. Buzug, "Dynamic single-domain particle model for magnetite particles with combined crystalline and shape anisotropy," *Journal of Physics D: Applied Physics*, vol. 48, no. 27, p. 275001, 2015.

[42] D. B. Reeves and J. B. Weaver, "Combined Néel and Brown rotational Langevin dynamics in magnetic particle imaging, sensing, and therapy," *Applied Physics Letters*, vol. 107, no. 22, p. 223106, 2015.

[43] C. Shasha, E. Teeman, and K. M. Krishnan, "Harmonic simulation study of simultaneous nanoparticle size and viscosity differentiation," *IEEE Magnetics Letters*, vol. 8, pp. 1–5, 2017.

[44] U. M. Engelmann, C. Shasha, E. Teeman, I. Slabu, and K. M. Krishnan, "Predicting size-dependent heating efficiency of magnetic nanoparticles from experiment and stochastic néel-brown langevin simulation," *Journal of Magnetism and Magnetic Materials*, vol. 471, pp. 450–456, 2019.

[45] H. Albers, T. Kluth, , and T. Knopp, "Simulating magnetization dynamics of large ensembles of single domain nanoparticles: Numerical study of

brown/néel dynamics and parameter identification problems in magnetic particle imaging," *Journal of Magnetism and Magnetic Materials*, vol. 541, p. 168508, 2022.

[46] H. Albers, T. Knopp, M. Möddel, M. Boberg, , and T. Kluth, "Modeling the magnetization dynamics for large ensembles of immobilized magnetic nanoparticles in multi-dimensional magnetic particle imaging," *Journal of Magnetism and Magnetic Materials*, vol. 543, p. 168534, 2022.

[47] J. Weizenecker, "The fokker-planck equation for coupled brown-néel-rotation," *Phys. Med. Biol.*, vol. 63, no. 3, p. 035004, 2018.

[48] A. Alpman, M. Utkur, and E. U. Saritas, "Mnp characterization and signal prediction using a model-based dictionary," *Int. J. Mag. Part. Imag.*, vol. 8, no. 1, p. 035004, 2022.

[49] T. Knopp, T. F. Sattel, S. Biederer, J. Rahmer, J. Weizenecker, B. Gleich, J. Borgert, and T. M. Buzug, "Model-based reconstruction for magnetic particle imaging," *IEEE Transactions on Medical Imaging*, vol. 29, no. 1, pp. 12–18, 2010.

[50] C.-Y. Hong, C. C. Wu, Y. C. Chiu, S. Y. Yang, H. E. Horng, and H. C. Yang, "Magnetic susceptibility reduction method for magnetically labeled immunoassay," *Applied Physics Letters*, vol. 88, p. 212512, 05 2006.

[51] C. C. Yang, S. Y. Yang, H. H. Chen, W. L. Weng, H. E. Horng, J. J. Chieh, C. Y. Hong, and H. C. Yang, "Effect of molecule-particle binding on the reduction in the mixed-frequency alternating current magnetic susceptibility of magnetic bio-reagents," *Journal of Applied Physics*, vol. 112, p. 024704, 07 2012.

[52] K. Wu, D. Su, R. Saha, J. Liu, V. K. Chugh, and J.-P. Wang, "Magnetic particle spectroscopy: A short review of applications using magnetic nanoparticles," *ACS Applied Nano Materials*, vol. 3, no. 6, pp. 4972–4989, 2020.

[53] M. Utkur, Y. Muslu, and E. U. Saritas, "Relaxation-based viscosity mapping for magnetic particle imaging," *Physics in Medicine & Biology*, vol. 62, no. 9, p. 3422, 2017.

[54] F. Weigl, A. Seifert, A. Kraupner, M. Jakob Peter, K.-H. Hiller, and F. Fidler, "Evaluating blood clot progression using magnetic particle spectroscopy," *International Journal on Magnetic Particle Imaging*, vol. 3, no. 1, 2017.

[55] H. Khurshid, Y. Shi, B. L. Berwin, and J. B. Weaver, "Evaluating blood clot progression using magnetic particle spectroscopy," *Medical Physics*, vol. 45, no. 7, pp. 3258–3263, 2018.

[56] F. Fidler, M. Steinke, A. Kraupner, C. Grüttner, K.-H. Hiller, A. Briel, F. Westphal, H. Walles, and P. M. Jakob, "Stem cell vitality assessment using magnetic particle spectroscopy," *IEEE Transactions on Magnetics*, vol. 51, no. 2, pp. 1–4, 2015.

[57] W. C. Poller, N. Löwa, F. Wiekhorst, M. Taupitz, S. Wagner, K. Möller, G. Baumann, V. Stangl, L. Trahms, and A. Ludwig, "Magnetic particle spectroscopy reveals dynamic changes in the magnetic behavior of very small superparamagnetic iron oxide nanoparticles during cellular uptake and enables determination of cell-labeling efficacy," *J. Biomed. Nanotechnol.*, vol. 12, no. 2, pp. 337–346, 2016.

[58] C. Gräfe, I. Slabu, F. Wiekhorst, C. Bergemann, F. von Eggeling, A. Hochhaus, L. Trahms, and J. H. Clement, "Magnetic particle spectroscopy allows precise quantification of nanoparticles after passage through human brain microvascular endothelial cells," *Physics in Medicine & Biology*, vol. 61, no. 11, p. 3986, 2016.

[59] H. Paysen, N. Loewa, A. Stach, J. Wells, O. Kosch, S. Twamley, M. R. Makowski, T. Schaeffter, A. Ludwig, and F. Wiekhorst, "Cellular uptake of magnetic nanoparticles imaged and quantified by magnetic particle imaging," *Sci. Rep.*, vol. 10, no. 1, p. 1922, 2020.

[60] Z. W. Tay, P. W. Goodwill, D. W. Hensley, L. Taylor, B. Zheng, and S. M. Conolly, "A high-throughput, arbitrary -waveform, mpi spectrometer and relaxometer for comprehensive magnetic particle optimization and characterization," *Sci. Rep.*, vol. 6, no. 1, p. 34180, 2016.

[61] W. Coffey, Y. Kalmykov, and J. Waldron, *The Langevin Equation: With Applications to Stochastic Problems in Physics, Chemistry and Electrical Engineering*. 09 2004.

[62] L. R. Croft, P. W. Goodwill, and S. M. Conolly, "Relaxation in x-space magnetic particle imaging," *IEEE Transactions on Medical Imaging*, vol. 31, no. 12, pp. 2335–2342, 2012.

[63] R. Rosensweig, "Heating magnetic fluid with alternating magnetic field," *Journal of Magnetism and Magnetic Materials*, vol. 252, pp. 370–374, 2002. Proceedings of the 9th International Conference on Magnetic Fluids.

[64] R. J. Deissler, Y. Wu, and M. A. Martens, "Dependence of brownian and néel relaxation times on magnetic field strength," *Med. Phys.*, vol. 41, no. 1, p. 012301, 2014.

[65] Y. Muslu, M. Utkur, O. B. Demirel, and E. U. Saritas, "Calibration-free relaxation-based multi-color magnetic particle imaging," *IEEE Transactions on Medical Imaging*, vol. 37, no. 8, pp. 1920–1931, 2018.

[66] P. Langevin, "On the theory of brownian motion," *Correspondences of the Royal Academy of Science (Paris)*, 1908.

[67] D. B. Reeves, *Nonequilibrium Dynamics of Magnetic Nanoparticles in Biomedical Applications*. Phd thesis, Dartmouth College, 2015.

[68] C. Shasha, *Nonequilibrium nanoparticle dynamics for the development of Magnetic Particle Imaging*. Phd thesis, University of Washington, 2019.

[69] O. Reynolds, "Xxix. an experimental investigation of the circumstances which determine whether the motion of water shall be direct or sinuous, and of the law of resistance in parallel channels," *Philosophical Transactions of the Royal Society of London*, vol. 174, pp. 935–982, 1883.

[70] J. B. MARION, "Chapter 10 - central-force motion," in *Classical Dynamics of Particles and Systems* (J. B. MARION, ed.), pp. 267–314, Academic Press, 1965.

[71] T. Gilbert, "A phenomenological theory of damping in ferromagnetic materials," *IEEE Transactions on Magnetics*, vol. 40, no. 6, pp. 3443–3449, 2004.

[72] N. Peskov, "Finite element solution of the fokker–planck equation for single domain particles," *Physica B: Condensed Matter*, vol. 599, p. 412535, 2020.

[73] M. I. Shliomis and V. I. Stepanov, *Theory of the Dynamic Susceptibility of Magnetic Fluids*, pp. 1–30. John Wiley & Sons, Ltd, 1994.

[74] D. Eberbeck, C. L. Dennis, N. F. Huls, K. L. Krycka, C. Gruttner, and F. Westphal, "Multicore magnetic nanoparticles for magnetic particle imaging," *IEEE Transactions on Magnetics*, vol. 49, no. 1, pp. 269–274, 2013.

[75] F. Ludwig, C. Balceris, C. Jonasson, and C. Johansson, "Analysis of ac susceptibility spectra for the characterization of magnetic nanoparticles," *IEEE Transactions on Magnetics*, vol. 53, no. 11, pp. 1–4, 2017.

[76] F. Ahrentorp, A. Astalan, J. Blomgren, C. Jonasson, E. Wetterskog, P. Svedlindh, A. Lak, F. Ludwig, L. J. van IJzendoorn, F. Westphal, C. Grüttner, N. Gehrke, S. Gustafsson, E. Olsson, and C. Johansson, "Effective particle magnetic moment of multi-core particles," *Journal of Magnetism and Magnetic Materials*, vol. 380, p. 221–226, 2015.

[77] K. Them, "On magnetic dipole–dipole interactions of nanoparticles in magnetic particle imaging," *Physics in Medicine and Biology*, vol. 62, no. 14, p. 5623–5639, 2017.

[78] Z. Zhao, N. Garraud, D. P. Arnold, and C. Rinaldi, "Effects of particle diameter and magnetocrystalline anisotropy on magnetic relaxation and magnetic particle imaging performance of magnetic nanoparticles," *Physics in Medicine and Biology*, vol. 65, no. 2, p. 025014, 2020.

[79] N. Cheng, "Formula for the viscosity of glycerol water mixture," *Industrial Engineering Chemistry Research*, vol. 47, no. 9, pp. 3285–3288, 2008.

[80] M. T. Arslan, A. A. Özaslan, S. Kurt, Y. Muslu, and E. U. Saritas, “Rapid taurus for relaxation-based color magnetic particle imaging,” *IEEE Transactions on Medical Imaging*, vol. 41, no. 12, pp. 3774–3786, 2022.

[81] Y. Wei, X. Li, L. Lin, D. Zhu, and Q. Li, “Causal discovery on discrete data via weighted normalized wasserstein distance,” *IEEE Trans. Neural Netw. Learn. Syst.*, 2022.

[82] F. Ludwig, T. Wawrzik, T. Yoshida, N. Gehrke, A. Briel, D. Eberbeck, and M. Schilling, “Optimization of magnetic nanoparticles for magnetic particle imaging,” *IEEE Transactions on Magnetics*, vol. 48, no. 11, pp. 3780–3783, 2012.

[83] T. Yoshida, N. B. Othman, and K. Enpuku, “Characterization of magnetically fractionated magnetic nanoparticles for magnetic particle imaging,” *Journal of Applied Physics*, vol. 114, p. 173908, 11 2013.

[84] S. Ota, Y. Matsugi, T. Nakamura, R. Takeda, Y. Takemura, I. Kato, S. Nohara, T. Sasayama, T. Yoshida, and K. Enpuku, “Effects of size and anisotropy of magnetic nanoparticles associated with dynamics of easy axis for magnetic particle imaging,” *Journal of Magnetism and Magnetic Materials*, vol. 474, pp. 311–318, 2019.

[85] D. Eberbeck, F. Wiekhorst, S. Wagner, and L. Trahms, “How the size distribution of magnetic nanoparticles determines their magnetic particle imaging performance,” *Applied Physics Letters*, vol. 98, p. 182502, 05 2011.

[86] Z. W. Tay, S. Savliwala, D. W. Hensley, K. L. B. Fung, C. Colson, B. D. Fellows, X. Zhou, Q. Huynh, Y. Lu, B. Zheng, P. Chandrasekharan, S. M. Rivera-Jimenez, C. M. Rinaldi-Ramos, and S. M. Conolly, “Superferromagnetic nanoparticles enable order-of-magnitude resolution & sensitivity gain in magnetic particle imaging,” *Small Methods*, vol. 5, no. 11, p. e2100796, 2021.

[87] F. Thieben, T. Knopp, M. Boberg, F. Foerger, M. Graeser, and M. Möddel, “On the receive path calibration of magnetic particle imaging systems,”

IEEE Transactions on Instrumentation and Measurement, vol. 72, pp. 1–15, 2023.

[88] O. L. Lanier, O. I. Korotych, A. G. Monsalve, D. Wable, S. Savliwala, N. W. F. Grooms, C. Nacea, O. R. Tuitt, and J. Dobson, "Evaluation of magnetic nanoparticles for magnetic fluid hyperthermia," *Int. J. Hyperthermia*, vol. 36, no. 1, pp. 687–701, 2019.

[89] A. Neumann, S. Draack, F. Ludwig, and T. M. Buzug, "Parameter estimations of magnetic particles: A comparison between measurements and simulations," in *International Workshop on Magnetic Particle Imaging*, p. 79, 2019.

[90] A. I. Karimov, D. N. Butusov, and A. V. Tutueva, "Adaptive explicit-implicit switching solver for stiff odes," in *2017 IEEE Conference of Russian Young Researchers in Electrical and Electronic Engineering (EIConRus)*, pp. 440–444, 2017.

[91] T. Knopp, H. Albers, M. Grosser, M. Möddel, and T. Kluth, "Exploiting the fourier neural operator for faster magnetization model evaluations based on the fokker-planck equation," *International Journal on Magnetic Particle Imaging*, vol. 9, no. 1, 2023.

[92] M. Lakshmanan, "The fascinating world of the landau–lifshitz–gilbert equation: an overview," *Philosophical Transactions of the Royal Society A: Mathematical, Physical and Engineering Sciences*, vol. 369, no. 1939, pp. 1280–1300, 2011.

Appendix A

Appendix for Equation Derivations

A.1 Derivation of Langevin Function

One can assume, without loss of generality, that the applied magnetic field is in the z-direction $\boldsymbol{B} = B\boldsymbol{z}$ and θ is the angle between $\boldsymbol{m}$ and $\boldsymbol{z}$. Then, the energy for each MNP can be written as

$$E = -\boldsymbol{\mu} \cdot \boldsymbol{B} = -\mu B cos(\theta) = -\mu B x \tag{A.1}$$

where $x = cos(\theta)$. To find the mean alignment of the magnetic moment vectors with the applied field direction, one can calculate the mean x as follows:

$$\langle E \rangle = -\langle \mu B x \rangle = -\mu B \langle x \rangle \tag{A.2}$$

where $\langle \cdot \rangle$ denotes the mean operator. The probability of an MNP being in the energy state E is determined by the Boltzmann distribution, meaning that the probability is proportional to $\exp(-E/k_B T)$. Therefore, the partition function for the continuum of energy states is as follows:

$$\mathscr{Z} = \int \exp\left(-\frac{E}{k_B T}\right) dE \tag{A.3}$$

where k_B is the Boltzmann constant and T is the temperature. Then the average energy becomes:

$$\langle E \rangle = \frac{1}{\mathscr{Z}} \int E \exp\left(-\frac{E}{k_B T}\right) dE \tag{A.4}$$

Here, by defining a unitless variable $\xi = \frac{\mu B}{k_B T} = \frac{-E}{k_B T x}$, we can transform the above equation to the following:

$$\begin{aligned} \langle E \rangle &= \frac{1}{\mathscr{Z}} \int_{-1}^{1} -\xi k_B T x \exp(\xi x) \left(-\xi k_B T dx\right) \\ &= \frac{(\xi k_B T)^2}{\mathscr{Z}} \int_{-1}^{1} x \exp(\xi x)\, dx \end{aligned} \tag{A.5}$$

We can also write the partition function $\mathscr{Z}$ in terms of ξ as follows:

$$\mathscr{Z} = \int \exp\left(\frac{-E}{k_B T}\right) dE = \int_{-1}^{1} \exp(\xi x) \left(-\xi k_B T dx\right) = -\xi k_B T \int_{-1}^{1} \exp(\xi x)\, dx \tag{A.6}$$

Then, Eq. (A.5) becomes:

$$\begin{aligned} \langle E \rangle &= \frac{(\xi k_B T)^2}{\mathscr{Z}} \int_{-1}^{1} x \exp(\xi x)\, dx \\ &= \frac{(\xi k_B T)^2}{-\xi k_B T \int_{-1}^{1} \exp(\xi x)\, dx} \int_{-1}^{1} x \exp(\xi x)\, dx \\ &= \frac{-\xi k_B T}{\int_{-1}^{1} \exp(\xi x)\, dx} \int_{-1}^{1} x \exp(\xi x)\, dx \\ &= -\xi k_B T \frac{\int_{-1}^{1} x \exp(\xi x)\, dx}{\int_{-1}^{1} \exp(\xi x)\, dx} \end{aligned} \tag{A.7}$$

Remembering the relation between the energy and the magnetization (Eq. (A.2)), $\langle x \rangle$ becomes

$$
\begin{aligned}
-\mu B\langle x\rangle &= -\xi k_B T\frac{\int_{-1}^{1} x\exp(\xi x)\,dx}{\int_{-1}^{1}\exp(\xi x)\,dx}\\
\langle x\rangle &= \frac{\int_{-1}^{1} x\exp(\xi x)\,dx}{\int_{-1}^{1}\exp(\xi x)\,dx}\\
\langle x\rangle &= \coth(\xi)-\frac{1}{\xi}=\mathcal{L}(\xi)
\end{aligned} \tag{A.8}
$$

The overall sample magnetization can be obtained by multiplying $\langle x\rangle$ with the dipole magnetic moment as follows:

$$
M=\mu\rho\mathcal{L}(\xi) \tag{A.9}
$$

Here, M is the magnetization amplitude in the applied field direction, ρ is the particle density.

A.2 Derivation for Langevin Equation of Brownian Rotation

Remembering $\boldsymbol{\mu}=\mu\boldsymbol{m}$ and multiplying Equation (2.26) with $\boldsymbol{m}$ from right hand side, we have

$$
\begin{aligned}
6\eta V_h(\boldsymbol{\Omega}\times\boldsymbol{m}) &= (\boldsymbol{\mu}\times\boldsymbol{B})\times\boldsymbol{m}\\
6\eta V_h\frac{d\boldsymbol{m}}{dt} &= (\boldsymbol{\mu}\times\boldsymbol{B})\times\boldsymbol{m}
\end{aligned} \tag{A.10}
$$

As a result, we have:

$$
\frac{d\boldsymbol{m}}{dt}=\frac{M_sV_c}{6\eta V_h}\left[(\boldsymbol{m}\times\boldsymbol{B})\times\boldsymbol{m}\right] \tag{A.11}
$$

Using $\boldsymbol{\xi}=\frac{M_sV_c\boldsymbol{B}}{k_BT}$, we have

$$\frac{d\boldsymbol{m}}{dt} = \frac{1}{2\tau_B}\left[(\boldsymbol{m} \times \boldsymbol{\xi}) \times \boldsymbol{m}\right] \tag{A.12}$$

where τ_B is the Brownian relaxation time constant which is defined in Equation (2.9).

A.3 Derivation for Langevin Equation of Néel Rotation

One can iterate through $d\boldsymbol{m}/dt$ by writing the right-hand side of Eq. (2.37) in place of $d\boldsymbol{m}/dt$. This leads to the explicit form of Gilbert's equation as follows:

$$\begin{aligned}
\frac{d\boldsymbol{m}}{dt} &= -\gamma \boldsymbol{m} \times \boldsymbol{B} + \alpha \boldsymbol{m} \times \frac{d\boldsymbol{m}}{dt} && \text{(A.13)}\\
&= -\gamma \boldsymbol{m} \times \boldsymbol{B} + \alpha \boldsymbol{m} \times \left(-\gamma \boldsymbol{m} \times \boldsymbol{B} + \alpha \boldsymbol{m} \times \frac{d\boldsymbol{m}}{dt}\right) && \text{(A.14)}\\
&= -\gamma \boldsymbol{m} \times \boldsymbol{B} - \gamma\alpha \boldsymbol{m} \times (\boldsymbol{m} \times \boldsymbol{B}) + \alpha^2 \boldsymbol{m} \times \left(\boldsymbol{m} \times \frac{d\boldsymbol{m}}{dt}\right) && \text{(A.15)}\\
&= -\gamma \boldsymbol{m} \times \boldsymbol{B} - \gamma\alpha \boldsymbol{m} \times (\boldsymbol{m} \times \boldsymbol{B}) - \alpha^2 \frac{d\boldsymbol{m}}{dt} && \text{(A.16)}
\end{aligned}$$

To go from Eq. (A.15) to (A.16), we used $\boldsymbol{a} \times (\boldsymbol{b} \times \boldsymbol{c}) = \boldsymbol{b}(\boldsymbol{c} \cdot \boldsymbol{a}) - \boldsymbol{c}(\boldsymbol{a} \cdot \boldsymbol{b})$ and the fact that $d\boldsymbol{m}/dt$ is orthogonal to $\boldsymbol{m}$, deduced from Equation (2.34), yielding the following:

$$\begin{aligned}
\boldsymbol{m} \times \left(\boldsymbol{m} \times \frac{d\boldsymbol{m}}{dt}\right) &= \boldsymbol{m}\left(\frac{d\boldsymbol{m}}{dt} \cdot \boldsymbol{m}\right) - \frac{d\boldsymbol{m}}{dt}(\boldsymbol{m} \cdot \boldsymbol{m})\\
&= -\frac{d\boldsymbol{m}}{dt}(\boldsymbol{m} \cdot \boldsymbol{m})\\
&= -\frac{d\boldsymbol{m}}{dt}
\end{aligned} \tag{A.17}$$

As a result, we have:

$$\frac{d\boldsymbol{m}}{dt} = \frac{-\gamma}{1+\alpha^2}\left[\boldsymbol{m} \times \boldsymbol{B} + \alpha \boldsymbol{m} \times (\boldsymbol{m} \times \boldsymbol{B})\right] \tag{A.18}$$

This is the Landau-Lifshitz-Gilbert (LLG) equation [92]. Note that with the following conversion of the parameters, Landau-Lifshitz (2.35) and LLG equations (A.18) become the same.

$$\gamma' = \frac{\gamma}{1+\alpha^2} \quad \mathscr{K} = \frac{\gamma\alpha}{(1+\alpha^2)} \tag{A.19}$$

Rewriting Equation (A.18), we have

$$2\tau_N \frac{d\boldsymbol{m}}{dt} = \frac{-V_c}{kT}\left[\frac{1}{\alpha}\boldsymbol{m}\times\boldsymbol{B} + \boldsymbol{m}\times(\boldsymbol{m}\times\boldsymbol{B})\right] \tag{A.20}$$

A.4 Derivation of Brownian FPE

Substituting Eq. (A.12) to (2.43), we have

$$\frac{\partial f(\theta,\phi,t)}{\partial t} = -\nabla\cdot\left(\frac{(\boldsymbol{m}\times\boldsymbol{\xi})\times\boldsymbol{m}}{2\tau_B} - D\nabla\right) f(\theta,\phi,t) \tag{A.21}$$

Using BAC-CAB rule, we have

$$\frac{\partial f(\theta,\phi,t)}{\partial t} = -\nabla\cdot\left(\frac{\boldsymbol{\xi} - \boldsymbol{m}(\boldsymbol{m}\cdot\boldsymbol{\xi})}{2\tau_B} - D\nabla\right) f(\theta,\phi,t) \tag{A.22}$$

We can select the direction of the applied field as $\hat{\boldsymbol{z}}$ without loss of generality. Then, the expression will only depend on the polar angle (θ) and the divergence will give the following:

$$\frac{\partial f(\theta,t)}{\partial t} = \frac{1}{\sin\theta}\frac{\partial}{\partial\theta}\left[\sin\theta\left(-\frac{\xi\sin\theta}{2\tau_B}f(\theta,t) + D\frac{\partial f(\theta,t)}{\partial\theta}\right)\right] \tag{A.23}$$

Replacing $x = \cos\theta$, we have:

$$2\tau_B\frac{\partial f(\theta,t)}{\partial t} = \frac{\partial}{\partial x}\left[(1-x^2)\left(\frac{\partial f(\theta,t)}{\partial x} - \xi(t)f(\theta,t)\right)\right], \tag{A.24}$$

This resulting partial differential equation is FPE for Brownian rotation of MNPs with uniaxial symmetry.

A.5 Derivation for Brownian FPE Solution

The following properties of the Legendre polynomials will be useful while solving Equation (A.24).

$$\frac{\mathrm{d}}{\mathrm{d}x}\left[(1-x^2)\frac{\mathrm{d}P_n}{\mathrm{d}x}\right] = -n(n+1)P_n \tag{A.25}$$

$$(1-x^2)\frac{\mathrm{d}P_n}{\mathrm{d}x} = nP_{n-1} - nxP_n \tag{A.26}$$

$$xP_n = \frac{(n+1)P_{n+1} + nP_{n-1}}{(2n+1)} \tag{A.27}$$

$$\int_{-1}^{1} P_n(x)P_m(x)dx = \frac{2}{2n+1}\delta_{mn} \tag{A.28}$$

Inserting Equation (2.46) into Equation (A.24), we have:

$$2\tau_B \sum_{n=0}^{\infty} P_n(x)\frac{\mathrm{d}a_n(t)}{\mathrm{d}t} = \sum_{n=0}^{\infty} a_n(t)\frac{\mathrm{d}}{\mathrm{d}x}\left[(1-x^2)\left(\frac{\mathrm{d}P_n(x)}{\mathrm{d}x} - \xi(t)P_n(x)\right)\right] \tag{A.29}$$

Using Property A.25 and derivative of product rule, we have;

$$\begin{aligned} &2\tau_B \sum_{n=0}^{\infty} P_n(x)\frac{\mathrm{d}a_n(t)}{\mathrm{d}t} = \\ &\sum_{n=0}^{\infty} a_n(t)\left[(-n(n+1)P_n(x)) - \left[(-2x)\xi(t)P_n(x) + (1-x^2)\xi(t)\frac{\mathrm{d}P_n(x)}{\mathrm{d}x}\right]\right] \end{aligned} \tag{A.30}$$

Utilizing Property A.26 leads to:

$$2\tau_B \sum_{n=0}^{\infty} P_n(x) \frac{\mathrm{d}a_n(t)}{\mathrm{d}t} =$$

$$\sum_{n=0}^{\infty} a_n(t) \Big[(-n(n+1)P_n) - \big[(-2x)\xi(t)P_n + \xi(t)(nP_{n-1} - nxP_n) \big] \Big] \quad \text{(A.31)}$$

$$= \sum_{n=0}^{\infty} a_n(t) \Big[P_n\big(-n(n+1) + \xi(t)(n+2)x \big) - \xi(t)nP_{n-1} \Big] \quad \text{(A.32)}$$

Using Property A.27 yields that:

$$2\tau_B \sum_{n=0}^{\infty} P_n(x) \frac{\mathrm{d}a_n(t)}{\mathrm{d}t} =$$

$$= \sum_{n=0}^{\infty} a_n(t) \Big[-P_n n(n+1) + \xi(t)(n+2) \left(\frac{(n+1)P_{n+1} + nP_{n-1}}{2n+1} \right) \quad \text{(A.33)}$$

$$- \xi(t)nP_{n-1} \Big]$$

$$= \sum_{n=0}^{\infty} a_n(t) \Big[-P_n n(n+1) + \xi(t)P_{n+1} \left(\frac{(n+1)(n+2)}{2n+1} \right) - \quad \text{(A.34)}$$

$$\xi(t)P_{n-1} \left(\frac{n(n-1)}{2n+1} \right) \Big]$$

Multiplying both sides by P_m, integrating over the interval $(-1, 1)$, and utilizing Property A.28, we obtain:

$$2\tau_B \frac{2}{2m+1} \frac{\mathrm{d}a_m}{\mathrm{d}t} = -\frac{2}{2m+1} m(m+1)a_m + \xi(t) \frac{2}{2m+1} \frac{m(m+1)}{2m-1} a_{m-1} \quad \text{(A.35)}$$

$$- \xi(t) \frac{2}{2m+1} \frac{m(m+1)}{2m+3} a_{m+1}$$

As a result, we can obtain the following ODE of coefficients:

$$\frac{\mathrm{d}a_m}{\mathrm{d}t} = \frac{m(m+1)}{2\tau_B} \left[-a_m + \xi(t) \left[\frac{a_{m-1}}{2m-1} - \frac{a_{m+1}}{2m+3} \right] \right] \quad \text{(A.36)}$$